Experimental Investigation of Hydraulic Fracturing and Stress Sensitivity of Fracture Permeability under changing Polyaxial Stress Conditions

Experimental Investigation of Hydraulic Fracturing and Stress Sensitivity of Fracture Permeability under Changing Polyaxial Stress Conditions

*** A. P. Fraser-Harris[1], C. I. McDermott[1], G. D. Couples[2], K. Edlmann[1], A. Lightbody[1], A. Cartwright-Taylor[1], J. E. Kendrick[1], F. Brondolo[1,3], M. Fazio[4], and M. Sauter[4]**

[1] School of Geosciences, University of Edinburgh, James Hutton Road, Edinburgh EH9 3FE

[2] Institute for Geoenergy Engineering, Heriot Watt University, Edinburgh, EH14 4AS

[3] now at Stanford Synchrotron Radiation Lightsource, SLAC National Accelerator Laboratory, 2575 Sand Hill Road, Menlo Park, CA 94025, USA

[4] Department of Applied Geology, Geoscience Centre of the University of Göttingen, Goldschmidtstraße 3, 37077 Göttingen, Germany.

Corresponding author: Andrew Fraser-Harris (*a.p.fraser-harris@ed.ac.uk)

†Additional author notes should be indicated with symbols (for example, for current addresses).

Key Points:

- Hydraulic stimulation, monitored with fibre optic strain sensors, shows both stable and unstable fracture propagation.
- Controlled polyaxial stress with rotatable radial stresses are used to interrogate normal and shear stress controls on fracture fluid flow.
- Fracture-normal effective stress exerts first order control on fracture permeability but increasing offset can lead to elevated permeability.

Keywords:

Hydraulic stimulation, Fracture fluid flow, Triaxial stress, True-triaxial stress, Polyaxial stress, Permeability

Abstract

Understanding and predicting fracture propagation and subsequent fluid flow characteristics is critical to geoenergy technologies that engineer and/or utilise favourable geological conditions to store or extract fluids from the subsurface. Fracture permeability decreases non-linearly with increasing normal stress, but the relationship between shear displacement and fracture permeability is less well understood. We utilise the new **G**eo-**R**eservoir **E**xperimental **A**nalogue **T**echnology (GREAT cell), which can apply polyaxial stress states and realistic reservoir temperatures and pressures to cylindrical samples, and has the unique capability to alter both the magnitude and orientation of the radial stress field by increments of 11.25° during an experiment. We load synthetic analogue materials and real rock samples to stress conditions representative of 500 - 1000 m depth, investigate the hydraulic stimulation process, and then conduct flow experiments whilst changing the fluid pressure and the orientation of the intermediate and minimum principal stresses. High-resolution circumferential strain measurements combined with fluid pressure data indicate fracture propagation can be both stable (no fluid pressure drop) and unstable (fluid pressure drop). The induced fractures exhibit both opening and shear displacements during their creation and/or during fluid flow with changing radial stress states. Flow tests during radial stress field rotation reveal that fracture normal effective stress has first order control on fracture permeability but increasing fracture offset can lead to elevated permeabilities at maximum shear stress. The results have implications for our conceptual understanding of fracture propagation as well as fluid flow and deformation around fractures.

1. Introduction

The hydro-mechanical behaviour of rock fractures is of fundamental importance for a wide variety of subsurface applications. These include groundwater resources (Gaus & Ó Dochartaigh, 2000), geotechnical applications such as tunnel excavation (Bossart et al., 2002), radioactive waste disposal (Birkholzer et al., 2018; Fraser Harris et al., 2015; Hudson et al., 2005; McDermott et al., 2015), carbon capture and storage (McCraw et al., 2016; McDermott et al., 2016), energy storage (e.g. strategic gas storage, compressed air storage or hydrogen storage Bai et al., 2018; Heinemann et al., 2018; Kabuth et al., 2017), tight conventional and unconventional hydrocarbons (Aybar et al., 2014; Fatahi et al., 2017; Guo et al., 1993; Guo et al., 2014), and geothermal energy (Hu et al., 2020; McClure & Horne, 2014; McDermott et al., 2006; Tomac & Sauter, 2018). In low permeability rocks, extraction technologies such as unconventional hydrocarbons and geothermal energy, fractures represent desirable high permeability pathways that facilitate economic fluid flow. Where interconnected fracture networks do not occur naturally, or are unable to yield economically viable flow rates, stimulation mechanisms involving injecting pressurised fluid are used to either generate new fractures (hydraulic fracturing) or reactivate existing fractures (hydro-shearing) increase existing permeability

Many experimental studies have investigated the controlling factors on hydraulic fracture propagation including stress controls, injection parameters, and interactions with pre-existing features e.g. bedding planes or fractures. Stress controls on fracture propagation were first investigated by Hubbert & Willis (1957) who determined the expected orientation of fractures with respect to the tectonic stresses, assuming tensile (Mode I) failure. Experimental studies by Chitrala et al. (2013) have shown that both shear and tensile failure modes are common in hydraulic fracturing, as indicated by focal mechanism data from acoustic

emissions (AE), while Solberg et al. (1977) showed that whether shear or tensile failure were the dominant mechanism is stress ratio related. Warpinski et al. (1982) investigated the important behaviour of fracture containment due to stress contrasts, highlighting this as one of multiple factors controlling fracture containment via the arrest of fracture propagation. The main injection parameters of interest have been the fluid viscosity, pressurisation rate or injection rate, and more recently cyclic injection schemes. Ishida et al. (2004), Stanchits et al. (2015), Zoback et al. (1977) all show that high viscosity fluid is more likely to lead to stable fracture propagation based on the conceptual model that high viscosity fluids are unable to penetrate tight fractures to apply the fluid pressure at the fracture tip (Zoback et al., 1977). Pressurisation rate or injection rate has been shown to impact breakdown pressures, with higher rates leading to higher breakdown pressures e.g. (Cheng & Zhang, 2020; Haimson & Zhao, 1991; Lockner & Byerlee, 1977; Zhuang et al., 2018). In an attempt to reduce seismicity during hydraulic fracturing and improve efficiency, fatigue hydraulic fracturing through cyclic injection schemes has been proposed. Hofmann et al. (2018), Patel et al. (2017), Zhuang et al. (2020, 2019) introduced experimental and field work on cyclic injection schemes which reduce the breakdown pressure and reduce the maximum amplitude of associated acoustic emission (AE) events released by fracture generation. The final major area of research concerning fracture propagation has been the investigation of fracture propagation with respect to anisotropic mechanical properties and pre-existing interfaces such as natural fracture networks and bedding planes. Experimental and numerical research has shown that a larger differential horizontal stress magnitude induces dominant cross-cutting hydraulic fractures (Bahorich et al., 2012; Hou et al., 2014; Tan et al., 2017; Xu et al., 2015; Zhou et al., 2008). Cross-cutting fractures are also promoted by a high fracture approach angle (Blanton, 1982; Gu et al., 2012; Hou et al., 2014), high injection rate and low fluid viscosity (Beugelsdijk et al., 2000; de Pater & Beugelsdijk, 2005; Fan & Zhang, 2014; Lee et al., 2014; Zhou et al., 2008), and high shear strength or narrow cemented fractures (Bahorich et al., 2012; Lee et al., 2014; Sarmadivaleh, 2012; Tan et al., 2017; Zhou et al., 2008). Other factors of interest are the ratio of the induced hydraulic fracture height to the existing discontinuity (Bahorich et al., 2012), anisotropy of laminated media (Tan et al., 2017; Xu et al., 2015), and the fracture density (Fan & Zhang, 2014). Due to the need to understand true triaxial stress state controls on fracture propagation orientation and interaction, the majority of experiments necessarily employ true triaxial testing equipment.

Fracture propagation can be inferred from CT scanning (Zhuang et al., 2020), thin section and image analysis (Patel et al., 2017), as well as post experimental destructive analysis using dyed fluid e.g. (Cheng & Zhang, 2020). However, these are all post-experimental analyses that do not capture the propagating fracture front. Fracture propagation is monitored better through using AEs to reconstruct time series 3D location maps (Hu et al. (2020) and Stanchits et al. (2015) are recent examples of this); however this is an incredibly time and labour intensive process. Potential for induced seismicity is often assessed through AE event rates and magnitude-frequency distributions (Benson et al., 2020; Gehne et al., 2019; Meng & De Pater, 2011). The majority of hydraulic fracture propagation investigations focus on the propagation mechanisms, using these methods to better understand the fracture geometries and networks produced, as well as the likely fracture extent. AEs are also used to show the accumulation of damage during cyclic injection prior to fracture propagation (Diaz et al., 2020; Zhuang et al., 2020). In some cases following breakdown when fluid injection is sustained, AEs have been recorded at stable fluid pressures e.g. Hu et al. (2020). In these

situations it is not possible to ascertain the exact origin of these AEs, as they could be a consequence of fracture slip, fracture closure/opening, and/or stable fracture propagation. We investigate an alternative monitoring technique using fibre optic strain sensors to observe in real-time the propagating fracture front.

Here we utilise the Geo-Reservoir Experimental Analogue Technology (GREAT cell) that is capable of generating hydraulic fractures under polyaxial stress conditions and maintaining a hydraulic seal when the propagating fracture reaches the sample edge. We monitor hydraulic fracture propagation in both synthetic and real rock samples by employing fibre optic strain sensors attached to the circumference of the sample. These provide circumferential strain data around the sample with localised strain measurements every ~2.6 mm to a resolution of 1 micro-strain at a frequency of 25 Hz. Circumferential strain has previously been measured using extensometers (e.g. Hofmann et al., (2016)) but these only provide total/bulk circumferential strain. Our novel approach, facilitated by the cylindrical design of the polyaxial GREAT cell, allows us to detail localised deformation associated with fracture propagation events and their relation to fluid injection pressure to ascertain if stable or unstable fracture propagation is occurring.

The aim of hydraulic stimulation for either unconventional hydrocarbons extraction or EGS is to increase fluid flow to production wells in the subsurface through enhanced/generated fracture permeability. Experimental and numerical investigations of fracture permeability are an incredibly active area of current research and represent many challenges. In its simplest form, fracture permeability can be estimated from the fracture aperture (space between the two fracture surfaces) by approximating the fracture surfaces to two parallel plates (Witherspoon et al., 1980; Zimmerman & Main, 2003; Zimmerman & Bodvarsson, 1996). However, fractures are not simply planar parallel plates, and many authors have shown that taking the mean mechanical aperture (determined from fracture surface characteristics and used to represent the aperture between parallel plates) will not result in an accurate prediction of fluid flow (Kulatilake et al., 2008; Renshaw, 1995). The topography of fracture surfaces leads to significantly more complex behaviours, such as channelization (e.g. Guo et al., 2016; McDermott et al., 2015), non-linear flow (Konzuk & Kueper, 2004; Zhang & Nemcik, 2013; Zhou et al., 2015), non-linear relationships between fracture normal stress and effective hydraulic aperture (e.g. Bandis et al., 1983; Barton et al., 1985; Pyrak-Nolte et al., 1987; Witherspoon et al., 1980; Zimmerman & Main, 2003), and potential effective hydraulic aperture change when displacement juxtaposes fracture surface asperities (Chen et al., 2000; Lee & Cho, 2002; Shen et al., 2020; Vogler et al., 2016).

Of particular interest in unconventional hydrocarbons and EGS is the fluid flow response to fracture normal stress and shear displacement behaviours. To investigate fracture normal stress relationships with permeability, many researchers conducted uniaxial experiments (stress applied in axial direction either with or without jacketing the sample) to show that increasing normal stress leads to a decrease in permeability (Barton et al., 1985; Gale, 1982; Pyrak-Nolte et al., 1987; Witherspoon et al., 1980). This has particular importance when trying to understand fracture closure during the production phase from unconventional hydrocarbons (Iriarte et al., 2018). Witherspoon et al (1980) used this methodology to validate the cubic law for normal stresses below 20 MPa. Durham (1997) used a triaxial rig to perform fracture closure experiments under hydrostatic stress conditions on a fractured sample from the KTB geothermal site and Lamur et al., (2017) investigated fractured samples

of different porosity under hydrostatic conditions. Both found a non-linear relationship between effective stress and permeability while Lamur et al., (2017) showed the greatest impact of fracture generation was on lower porosity samples. A similarly non-linear relationship was found when hydraulic properties during fracture closure were investigated with conventional triaxial experimental equipment on sandstone and shale fractures containing proppant (Iriarte et al., 2018).

Shear dilation refers to the increase in effective hydraulic aperture as a result of juxtaposing asperities on each side of the fracture being forced past each other by displacement of the fracture. Experimental investigations of this phenomenon include static fracture offset tests (Chen et al., 2000; Hofmann et al., 2016; Zhou et al., 2015), direct shear tests at constant shear displacement rates (Shen et al., 2020), increasing shear stress (Rutter & Mecklenburgh, 2018), and hydraulically induced dynamic shear tests (Ye & Ghassemi, 2018). Kamali & Ghassemi (2018) and Ye & Ghassemi (2019) also provide mechanisms and evidence of fracture displacement leading to enhanced permeability through increased fracture tip stresses and the coalescence of nearby fractures during shear displacement, as opposed to the enhancement of permeability of each individual fractures through shear dilation. However, a consensus on the impact of displacement on permeability is somewhat inconclusive as some authors indicate that at low fracture normal stresses fracture offset leads to shear dilation that increases fracture permeability (Lee & Cho, 2002; Ye & Ghassemi, 2018), but at higher fracture normal stresses, or when dynamic slip behaviour produces wear products, shear displacement reduces permeability (Rutter & Mecklenburgh, 2018; Shen et al., 2020). Nevertheless, recent re-analysis of a stimulation operation at Fenton Hills in the 1970s via numerical modelling suggests that "hydro-shearing" (inducing shear dilation) does have the potential to produce enhanced fracture network permeability without generating unacceptable levels of seismicity (Rinaldi & Rutqvist, 2019).

Here we investigate normal stress and fracture offset controls on fracture permeability in an entirely novel way. Utilising the unique capability of the GREAT cell, we rotate the anisotropic horizontal stresses in stages within a polyaxial stress field during a fluid flow experiment in hydraulically generated fractures in rock and synthetic materials to investigate the relationship between fracture permeability, normal stress, and fracture offset in a 3D stress field.

2. Materials and Methods

2.1. Experimental equipment

The **G**eo-**R**eservoir **E**xperimental **A**nalogue **T**echnology (GREAT) cell has been built within the context of a collaboration between the University of Edinburgh, University of Göttingen, and Heriot Watt University, with the aim of providing testing facilities for large, fractured-rock samples under near-natural stress conditions. GREAT is a novel experimental apparatus capable of creating controlled, user-defined polyaxial stress states in large (193.75 mm diameter, 190-205 mm length) cylindrical fractured-rock samples, with the option of flowing fluids under thermal reservoir conditions (McDermott et al., 2018). Figure 1 shows a schematic diagram of the GREAT cell set-up under isothermal conditions. Axial load is applied via the hydraulic press acting on a steel platen on the top of the sample, with a fixed basal platen on the cell pedestal providing the opposite reaction force. Radial stresses in the sample are induced by pressurizing eight independently controlled pairs of fluid-filled

bladders retained by recesses in the confining vessel. These bladders, termed Pressure Exerting Elements (PEEs), are separated from adjacent PEEs by Dynamic Sealing Strips (DSSs) to prevent "pressure cross-talk". A 2 mm thick Viton™ sheath placed between the sample and the PEEs and DSSs ensures a good hydraulic seal if the fractures propagate to the sides of the sample. Pressure control of each PEE pair by the hydraulic circuit depicted in Figure 1 provides the ability to rotate and/or change the radial stresses during an experiment, enabling an in-depth investigation of the effect of the state of stress on coupled processes of non-isothermal fluid flow as well as mass and heat transport in fractured-porous rock material. Further details on the cell design are given in McDermott et al. (2018).

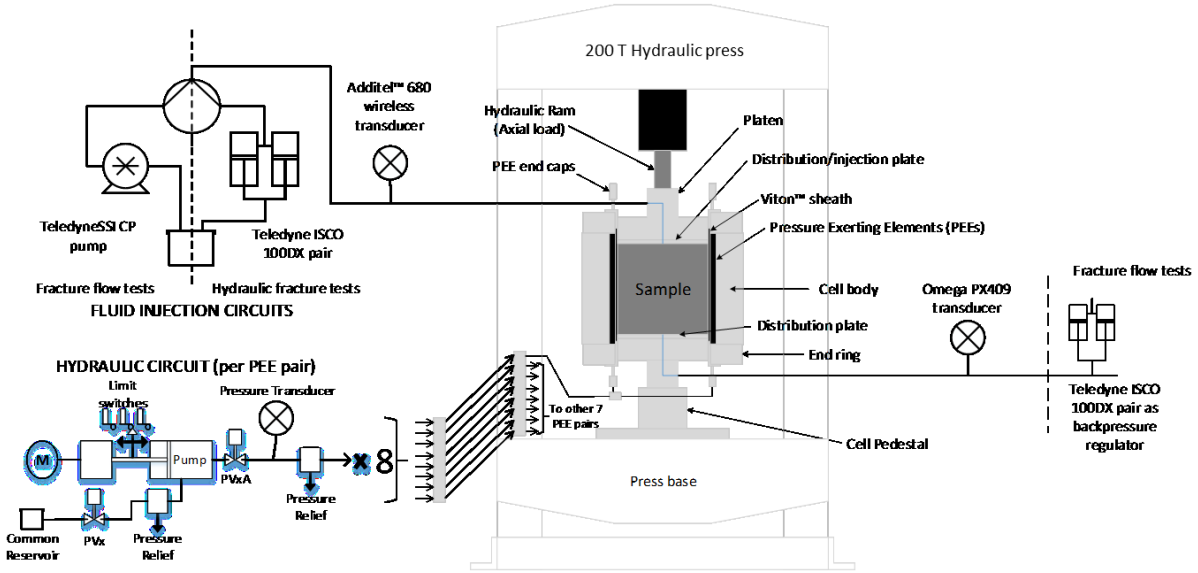

Figure 1: Schematic diagram of the GREAT cell set-up used in the presented experiments. Axial load is applied via the hydraulic ram, radial stresses in the sample are induced via the fluid pressure in the Pressure Exerting Element pairs generated by the hydraulic circuit, and fluid is injected into the intact or fractured sample through two optional pump arrangements depending on the test.

Fluid is injected into the cell through a central fluid port in the top platen (Figure 1). The system has two potential fluid injection options – a pair of Teledyne Isco 100DX pumps capable of a maximum pressure of 10,000 psi (68.95 MPa) and maximum flow rate of 50 ml/min used to generate hydraulic fractures, or a Scientific Systems Inc. Column Packing (CP) pump rated to 1000 psi (6.90 MPa) with a maximum flow rate of 300 ml/min. Fluid inlet pressure is recorded with a wireless Additel pressure transducer rated to 10,000 psi (68.95 MPa) in both pump configurations. There are also two options for downstream fluid pressure control - a manual backpressure regulator coupled with a an Omega PX409USB transducer rated to 1500 psi, or the pair of Teledyne Isco 100DX pumps in receive mode (to accurately monitor fluid flow rates when injecting with the SSI CP pump).

Strain data are recorded using a distributed fibre optic sensor produced by LUNA Technologies that uses Swept-Wavelength Interferometry to obtain strain data with a resolution of 1 με (Gifford et al., 2007). More information of the methodology and the advantages of this approach can be found in Gifford et al. (2007). The fibre is attached to the sample in a circumferential arrangement at the axial mid-point, providing a full recording of the strain at intervals of approximately 2.6 mm, providing 234 strain measurements. For

hydraulic fracturing data are recorded at 8 Hz (uniform resin) and 25Hz (heterogeneous resin and greywacke). Fracture fluid flow tests are recorded at 1 Hz.

2.2. Samples

To investigate both the creation of hydraulically generated fractures, and their subsequent permeability response under varying polyaxial stress conditions (rotating the radial stresses), we conduct a series of experiments on three cylindrical low permeability samples – two synthetic rock analogues, and a greywacke collected from the central belt of Scotland. In each case the samples are 193.75 mm in diameter, and 200 mm in length.

2.2.1. Synthetic samples

The two synthetic samples are transparent polyester resin and were prepared in-house by mixing water-clear polyester resin with MEKP catalyst at 1% concentration and casting in specially designed moulds of High Density Polyethylene (HDPE) in a series of pours (Fraser-Harris et al., 2020). The final diameter and parallel end faces are achieved on a workshop lathe.

Porosity was measured with a Micromeritics AccuPyc II 1340 helium pycnometer at the University of Liverpool on three polyester resin samples and found to have a mean of 0.16%, and a range between 0.08% and 0.22% (with an accuracy of +/- 0.05%, see supplementary information). The mechanical properties are a function of the accuracy of the fabrication process and, as such, there is a possible range of Young's Modulus between 3 - 4 GPa. This is based on literature data (Aly et al., 2010), modelling (3.85 GPa from McDermott et al., 2018), and in-house jacketed axial compression testing, which reveals a value of 3.11 GPa – close to the supplier data sheet value of 3.15 GPa. Poisson's ratio is taken to be 0.4 (Aly et al., 2010). The jacketed axial compression testing was conducted with the triaxial deformation rig in the NERC Experimental Geoscience Facility Rock Physics and Rock Deformation Laboratory at the University of Edinburgh on a standard sized sample (38 mm diameter, 95 mm length) using a 1 $x10^{-5}$ s^{-1} strain rate. The resin, confined to <0.1 MPa, yields and deforms visco-elastically at approximately 19 MPa (see supplementary information). As such, we remain below this value for hydraulic fracturing and fluid flow testing herein. Ultimate tensile strength (UTS) for a fully cured polyester resin given by the supplier is 40 MPa, although it is clearly stated that this is neither a minimum nor a maximum for the material due to potential variations in preparation. In addition, composites exhibit rate dependency (Lee, 2002), changing from visco-elastic behaviour to brittle failure with increasing strain. Brazilian tensile tests were conducted using an Instron 5969 uniaxial press at the Experimental Volcanology and Geothermal Research Laboratory at the University of Liverpool. Nine samples were deformed at three different equivalent diametric strain rates (three samples each at $1x10^{-2}$ s^{-1}, $1x10^{-3}$ s^{-1}, and $1x10^{-4}$ s^{-1}). Tests reveal that the polyester resin shows rate dependent behaviour, becoming more compliant but also stronger at slower strain rates. Mean Brazilian tensile strength from the two most consistent samples at each rate increases from 17.96 MPa, to 21.69 MPa, and to 27.31 MPa at $1x10^{-2}$ s^{-1}, $1x10^{-3}$ s^{-1}, and $1x10^{-4}$ s^{-1} respectively (see supplementary information).

Polyester resin is chosen for its ease of constructing samples, flexibility with respect to introducing heterogeneity during the construction, and its transparency that enables a clear observation and characterisation of the geometry of the fractures generated. As explained in Fraser-Harris et al. (2020), the construction of the resin samples is performed in small incremental pours to avoid heat damage (cracking of the resin as it cures). This process provides an opportunity to introduce contrasting materials at the interface between two successive pours, and to do so while also changing the angle of the mould so the orientation

of the new pour can be controlled (see heterogeneous resin image in Figure 2 for different orientations of heterogeneity). Using this necessary step-wise process to our advantage, we create mechanical heterogeneity in one resin sample by including a layer of 5 g of fine-grained sand (40-100 mesh size) on the interfaces between four pours. Using this method we introduce layers at 40 mm, 70 mm, 95 mm, 150 mm height from the base. In addition to the four horizontal layers (designed to simulate bedding planes), an inclined plane at 60° to horizontal is also included (Figure 2) to simulate the presence of a healed pre-existing fracture (or small fault). Sand-layers introduce mechanical heterogeneity but they do not affect the hydraulic properties of the encasing resin, and the evidence from the experiments reveals that the sand grains do not create a permeable pathway due to the complete encasement of each grain by the resin.

Each resin sample contains a 3 mm central bore 125 mm in length i.e. slightly more than half the sample length. This wellbore-like hole is for the fluid injection, and the length is designed to promote a fracture that initiates in the centre of the sample, growing to connect the injection point with the outlet at the base of the cell, to facilitate fracture flow experiments. Properties of the resin are summarised in Table 1.

2.2.2. Greywacke

The third sample is a low-porosity, low-permeability greywacke of the Eastgate Sandstone Member of the Silurian Westgate Formation obtained from a quarry in the central belt of Scotland, UK (Figure 2). It is composed of fine grained volcanic rock fragments, monocrystalline quartz, and subordinate plagioclase feldspar, as well as isolated large clasts of siltstone up to 45 mm in length, 20 mm in width. There is a <0.5 mm thick calcite vein that dips at approximately 83 degrees away from the central bore, starting at a distance of 38 mm from the bore at the top of the sample and intersecting the base of the sample 70 mm from the central axis. The greywacke sample preparation required the development of specific rock turning and grinding machinery designed and assembled in-house. The end faces were ground parallel and the diameter achieved by the newly designed up-right rock-turning rig (RTR) described in Fraser-Harris et al. (2020). A central borehole, 6 mm in diameter and 100 mm in length (due to available tooling) was drilled in the greywacke for fluid injection.

The greywacke is chosen for its extremely low connected porosity and corresponding low permeability, in order to minimize the contribution of matrix flow. Connected porosity was measured using the helium pycnometer at the University of Liverpool for 11 samples, with a mean connected porosity of 1.12% and a range of 0.73 to 1.47% (with an accuracy of +/- 0.05%). Based on the fractal adaptation of the Kozeny-Carmen model of Pape et al. (2000) for a shaley sandstone, matrix permeability is estimated to be 2.58×10^{-19} m^2 for the mean porosity of 1.12%. Due to the low connected porosity and permeability of the samples and the relatively short duration of the flow-through experiments in the generated fractures in this paper, (see section 2.4.3) we assume that the contribution of fluid flow in the matrix is negligible in comparison to fracture-hosted fluid flow. We therefore attribute calculated bulk permeability changes following changes in stress or fluid pressure to changes in the hydraulically-induced fracture(s) geometries.

Jacketed samples confined at <0.1 MPa were deformed axially in the triaxial deformation rig at the University of Edinburgh at a strain rate of 1×10^{-5} s^{-1} in two orthogonal orientations. Young's Modulus was determined to be 26.20 +/- 0.06 GPa (see supplementary information). Brazilian tensile tests were conducted using the Instron 5969 uniaxial press at the University of Liverpool. Six Brazilian tensile tests were performed at two equivalent diametric strain rates of 1×10^{-3} s^{-1} and 1×10^{-4} s^{-1} (three at each rate). Results show little rate dependency, with mean Brazilian tensile strengths from the two most consistent samples at each rate of 17.10

MPa and 16.67 MPa at $1x10^{-3}$ s^{-1} and $1x10^{-4}$ s^{-1}, respectively (one anomalously low strength was recorded, possibly due to an unseen defect in the sample; see supplementary information).

Table 1: Selected mechanical and petrophysical properties of the tested samples. The Young's Modulus of the resin is a calibrated value from numerical modelling (McDermott et al., 2018). Tensile strength for the resin reported here is the Brazilian tensile strength. Greywacke mechanical properties are determined from jacketed deformation tests and Brazilian tensile tests. Permeability of the greywacke is estimated from the model of Pape et al. (2000) for a shaley sandstone. *As discussed in the text, the tensile strength of the polyester resin was strongly rate dependent – the figures in this table are for $1x10^{-2}$ s^{-1} and $1x10^{-4}$ s^{-1} respectively. **These figures are for the two equivalent diametric strain rates of $1x10^{-3}$ s^{-1} and $1x10^{-4}$ s^{-1} respectively.

Sample type	Young's Modulus (GPa)	Poisson's Ratio	TS (MPa)	Porosity (%)	Permeability (estimated) (m^2)
Resin	3.85	0.40	17.96-25.08*	0.16	N/A
Greywacke	26.20	0.27	17.01-16.67**	1.12	$2.58x10^{-19}$

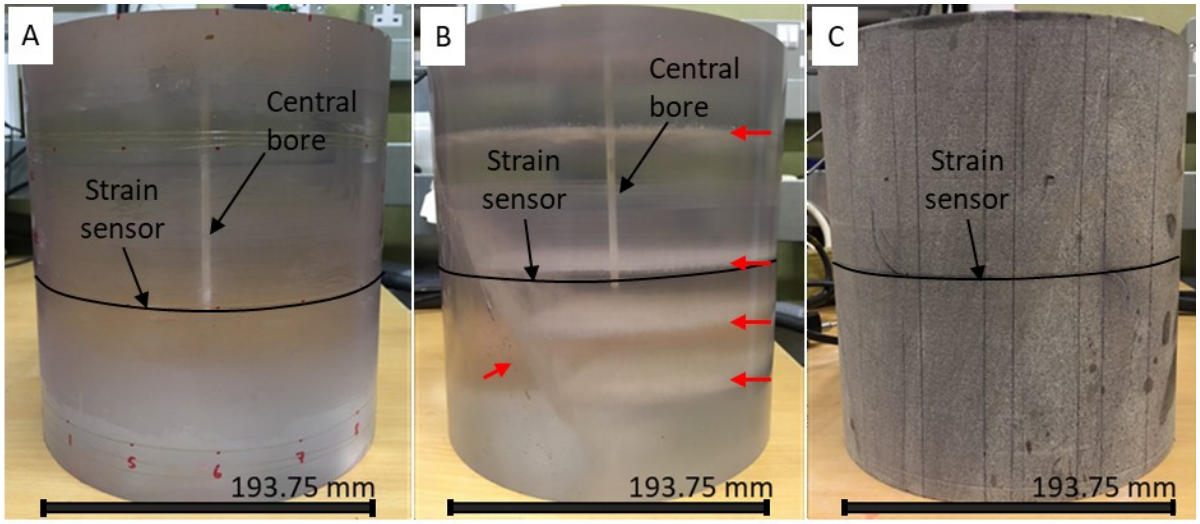

Figure 2: Samples for hydraulic fracturing experiments; A) uniform resin sample, B) heterogeneous resin sample with both horizontal and inclined planes (indicated by the red arrows), and C) greywacke.

2.3. Experimental Stress conditions

The target stresses for the experiments are shown in Table 2. For the polyester resins targets are: $\sigma_{axial} = \sigma_1 = 12$ MPa, $\sigma_2 = 7$ MPa, $\sigma_3 = 3$ MPa. For the fracture flow experiments with downstream pressure, the radial pressures are slightly higher ($\sigma_2 = 8$ MPa, $\sigma_3 = 4$ MPa) to enable a larger range of downstream pressures to be investigated. Target stresses are slightly larger for the greywacke sample to simulate depths of approximately 1 km ($\sigma_1 = 20$ MPa, $\sigma_2 = 15$ MPa, $\sigma_3 = 7$ MPa). Maximum principal stress is axial, so, based on standard theory, fracture propagation is expected to run parallel to both σ_1 and σ_2 (Hubbert & Willis, 1957). The experimental radial pressures in the PEEs around the sample circumference for the fracturing stage of each experiment are presented in Table 2. Pressure measurements in the PEEs are accurate to 0.1 MPa and automatically controlled to +/- 0.3 MPa around a set point. This can result in slight differences in boundary conditions depending on whether a bladder is increasing in pressure or decreasing towards the set point, as can be seen in Table 2 where the

365 set-points are shown in brackets. This equipment constraint is being addressed in ongoing
366 equipment upgrades.

367 **Table 2:** Table of the actual pressures of the Pressure Exerting Elements (PEEs) during each hydraulic fracturing test
368 compared to the target pressures in brackets. *σ_1 in each test is axial, **denotes σ_2 orientation, and ***denotes σ_3.

	Radial Pressure (MPa)		
	Test 1 Uniform Resin	Test 2 Heterogeneous Resin	Test 3 Greywacke
Axial	11.9 (12.0)*	12.0 (12.0)*	19.8 (20.0)*
PEE 1 & 1A	5.2 (5.0)	5.2 (5.0)	7.3 (7.0)***
PEE 2 & 2A	4.2 (4.0)	4.3 (4.0)	9.3 (9.0)
PEE 3 & 3A	3.3 (3.0)***	3.2 (3.0)***	11.3 (11.0)
PEE 4 & 4A	3.8 (4.0)	4.3 (4.0)	12.8 (13.0)
PEE 8 & 8A	4.9 (5.0)	5.1 (5.0)	14.8 (15.0)**
PEE 7 & 7A	5.7 (6.0)	5.8 (6.0)	12.9 (13.0)
PEE 6 & 6A	6.7 (7.0)**	6.8 (7.0)**	11.3 (11.0)
PEE 5 & 5A	5.7 (6.0)	5.9 (6.0)	9.3 (9.0)

369

370

371 ### 2.3.1. Stress conditions in the GREAT cell

372 In the experiments reported here, the GREAT cell has been utilised to induce a polyaxial
373 stress state within the sample. Due to the cylindrical shape, and the loads that we can apply
374 (only normal tractions on the circumference), it is not possible to achieve a uniform true-
375 triaxial state because of the inability to apply shear stresses on the sample margin in the radial
376 directions that lie in between the principal directions. Although there are no sensors located
377 within the sample at this stage of work, which could potentially demonstrate unequivocally
378 what stress states are created, numerical simulations of the loaded experiment (Figure 3)
379 show almost-true triaxial stress states within the sample (with small angular variations in
380 principal directions), but with non-uniform (but still polyaxial) stress magnitudes that vary
381 from the centre to the margins. Here we use these simulations to demonstrate the stress
382 conditions generated within the GREAT cell for given experimental boundary conditions.
383 Further modelling would be required to quantify the impact of these stress gradients on
384 hydraulic fracture propagation, yet, our simulations illustrate that the designed (far-field
385 loading) state is achieved in a quasi-rectangular region within the centre of the sample, with
386 departures from that near-uniform stress condition governed by the specific PEE pressure
387 assignments used in each experimental procedure. In the experiments presented here, we use
388 an opposing pair of PEEs to create the segments of radial principal stresses, and arrange a
389 linear variation of pressures in those PEEs located between the principal directions. A key
390 component of the experimental investigation is to utilise the capabilities of the GREAT cell

to rotate the created radial stress field during an experiment, and the same approximation to true-triaxial states will apply for these incrementally rotated conditions.

Using the linear elastic finite element model developed in McDermott et al (2018), the volume of the sample that is subjected to approximate true triaxial stress conditions is shown in Figure 3 i.e. within $\sigma_3 + 3\%$ and $\sigma_2 - 3\%$ of the first stress invariant ($I_1 = \sigma_1 + \sigma_2 + \sigma_3$) – a zone approximately 50 mm x 50 mm along the length of the sample. Here the stress states illustrated are those for the initial hydraulic fracturing stage of the uniform resin at the axial mid-point of the sample, using the values in Table 2. If induced fractures propagate from the central bore beyond this zone, they will encounter different (initial) stress conditions as they approach the sample margins. Although the propagation and subsequent presence of the fracture will change the stress field, the colder colours towards the sample edge along the *y=0* axis in Figure 3b, suggest that fractures propagating parallel to the intermediate principal stress will encounter an increasing value of the minimum principal stress (acting normal to that fracture plane) towards the sample edge. However, the shortest transport route through the fracture, and thus the part hosting the majority of fluid flow (assuming the largest aperture is near the fracture centre), is within this quasi-true triaxial zone. It is therefore reasonable to make an initial interpretation of the flow results based on these modelled true triaxial stress conditions.

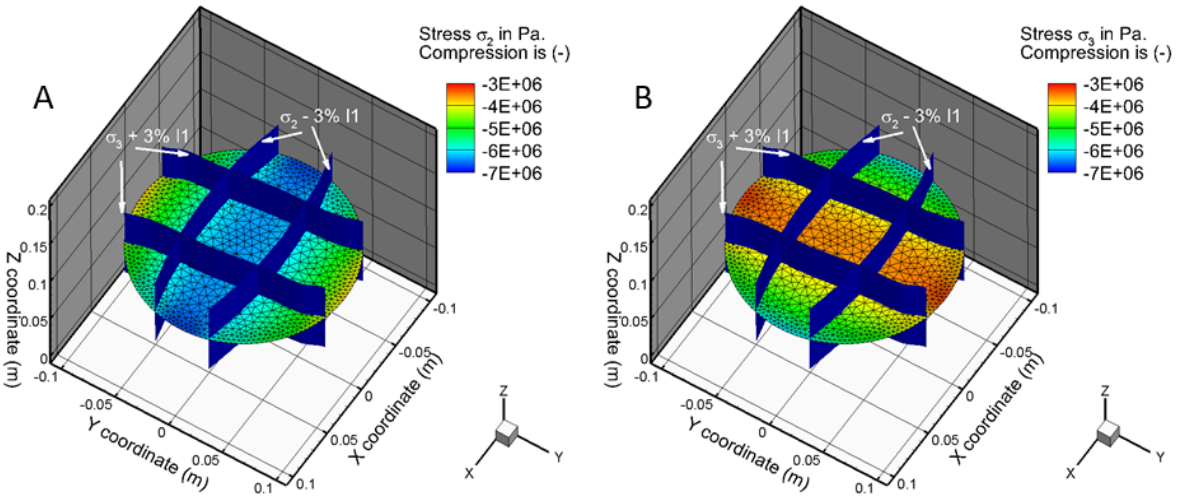

Figure 3: Linear elastic finite element models simulating the extent of the true triaxial zone in the cylindrical specimens tested in this paper; A) shows σ_2, B) shows σ_3. The approximately true triaxial zone (approximately 50 mm x 50 mm) is delimited by the iso-surfaces at σ_3 + 3% and σ_2 – 3% of the first stress invariant ($I1 = \sigma_1 + \sigma_2 + \sigma_3$). In these figures, the applied stresses of the uniform resin hydraulic fracturing experiment have been applied - σ_1 is axial, σ_2 is parallel to the *x*-axis, and σ_3 is parallel to the *y*-axis.

2.4. Experimental Protocol

Each experiment consists of a set-up loading phase, the experimental procedure (hydraulic fracturing and/or flow test), and the shut-down phase. Here we describe each in turn, and any variations with each test.

2.4.1. Sample loading

Two sample loading approaches are assessed as the experimental protocol is still being developed for the new GREAT cell within the limitations of the original control system. The

two resin samples are loaded axially to the target axial stress before the radial loads (in all PEEs) are uniformly raised to the maximum horizontal stress magnitude. The greywacke sample is loaded in stages under axisymmetric triaxial conditions i.e. both axial and radial stresses are raised together, with axial stress kept greater than the uniform radial stress (Figure 4) to prevent possible damage to the optical fibre strain sensor. Once the maximum horizontal stress is reached under axisymmetric triaxial conditions, the radial stress conditions are modified by reducing the pressure in appropriate PEEs to create the polyaxial stress conditions chosen for the experimental phase.

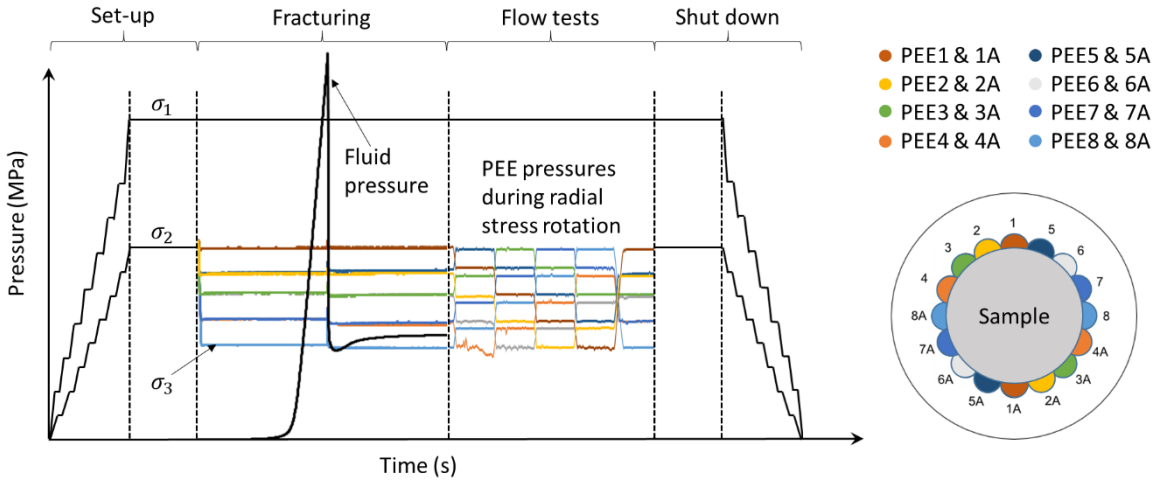

Figure 4: Schematic diagram of the experimental stages during the hydraulic fracturing experiments showing the set-up stages including conventional axisymmetric loading, hydraulic fracturing under polyaxial loading, fluid flow tests during radial stress rotation, and shutdown stages. In addition, a fluid injection profile for the hydraulic fracturing stage of the greywacke experiment in this paper (Section 3.1.3) is shown along with the PEE pressures during the static and changing true-triaxial stress conditions.

2.4.2. Hydraulic fracturing procedure

Once the experimental stress conditions have been established, each sample is hydraulically fractured in the GREAT cell by a constant-flow-rate fluid injection into the central, partially penetrating borehole (Figure 4). Fluid is injected with the pair of Teledyne Isco 100DX pumps, and fluid pressure is recorded with the wireless Additel pressure transducer (Figure 1). Following fracture propagation, fluid injection is continued for a nominal time until constant outflow is observed. During the hydraulic fracturing tests, the downstream pressure remains ambient (i.e. P = 1 bar).

Hydraulic fracturing is followed by the shutdown phase, in the resin samples, to visibly determine the orientation of the fracture before the sample is used for subsequent flow tests. In contrast, hydraulic fracturing of the greywacke sample is followed immediately by hydraulic flow tests, with shutdown occurring afterwards.

2.4.3. Hydraulic flow test procedure

In the hydraulic flow tests, normal and shear stresses are changed to determine their influence on fracture permeability. Each test consists of constant flow rate injection into the central borehole with a constant downstream pressure (at the sample's base, opposite to the injection that occurs from the top) for the duration of each test, under polyaxial stress conditions. Fluid is injected with the Scientific Systems Inc. Column Packing (CP) pump, and downstream

pressure is generated using the Teledyne Isco 100DX pumps in receive mode (Figure 1). Injection fluid pressure is recorded with the wireless Additel pressure transducer, while downstream pressure and flow rate are recorded by the Teledyne Isco 100DX pumps. During each test, the radial stress field is rotated in stages, such that the orientation of σ_2 and σ_3 rotate anti-clockwise by the angular difference of one PEE pair (22.5°). All pairs of PEEs changed simultaneously from their prior pressures during the few seconds taken to make these changes. During that short (approximately 2-5 seconds) transient stress state changeover, the fluid pressure data is not considered in the analysis of the fracture flow properties. The short stage length is designed to be long enough to establish flow parameters not affected by the process of the stress field rotation (Figure 4) but also to limit the impact of any geochemical reactions on the fresh fracture surface, especially for the greywacke.

2.4.3.1. Further tests in the heterogeneous resin

In addition to the above flow test procedure, in the heterogeneous resin sample this type of experiment was repeated for four downstream pressures (0.69 MPa, 1.38 MPa, 2.07 MPa, and 2.76 MPa). This is to explore the influence of changing fluid pressure on effective hydraulic fracture aperture, and to examine whether any effects are dependent on hydraulic fracture orientations within the 3D stress field.

2.4.4. Shutdown phase

A reversal of the set-up phase is employed as a shutdown phase. In each case the stress field is returned to an axisymmetric stress field and axial and radial pressures are lowered in stages with the axial pressure always exceeding the radial PEE pressures to protect both the PEEs and the optical fibre.

3. Results

In this section, the results of the hydraulic fracturing experiments are presented for each of the three samples in turn, summarising the experimental stress state created, the fluid pressure data, and the circumferential strain response of the sample. Fracture geometries depend on the sample type, sample heterogeneity, and stress field. The fracture configurations are discussed for each case. The hydraulic flow test data are interpreted in terms of derived fracture permeability, presented in the following section, along with discussion of the implications.

3.1. Hydraulic fracturing

In each sample, a σ_1-parallel fracture is generated that propagates to the full axial length of the sample, with different radial extents for each of the three experiments, thus creating a connected flow path from end-to-end approximately through the centre of the sample. High-spatial-resolution strain data is recorded around the circumference of each sample at the axial mid-point. During the injection, fluid pressure increases until breakdown and fracture propagation are achieved.

3.1.1. Uniform Resin Sample

The hydraulic fracturing of the uniform resin sample captures three distinct progressive fracturing events as the fracture propagates approximately parallel to the intermediate principal stress.

Figure 5 shows the experimentally applied radial pressures (A) and the corresponding circumferential strain (B) at PEE locations between 0 and 90° (see inset i in Figure 5B). Maximum horizontal stress is in the direction of 90°-270°, and minimum horizontal stress is aligned along 0°-180° (see inset i in Figure 5B). Figure 5 also shows the difference in strain as a consequence of axisymmetric and polyaxial stress states, possibly as a result of the reduction in mean stress as the sample changes from axisymmetric to the selected polyaxial stress conditions (created by reducing pressures in selected PEES). The PEE response to the hydraulic fracture propagation as the deformation of the sample causes a change in pressure of the pressurising fluid in the PEEs before the system automatically responds (Figure 5A). Parallel to the fracture (approximately 90°) there is a small reduction in PEE pressure initially, but elsewhere around the circumference there is an increase in PEE pressure (with maximum perturbations perpendicular to the fracture). This matches with the strain data (Figure 5B) as hydraulic fracturing causes a different strain response depending on the angular location of the strain measurement. Parallel to the fracture (approximately 90°) the strain data show an increase in contraction but a decrease at all other measurement location angles during the fracture propagation events. Following the completion of fracture propagation, the strain show a variable recovery around the circumference of the sample. There is a permanent contraction parallel to the maximum horizontal stress (approximately parallel to the fracture) but permanent elongation is observed (with increasing magnitudes) towards the minimum horizontal stress (approximately perpendicular to the fracture). This indicates the sample has changed from an ellipse to an extended ellipse with localised kinks parallel to the fracture (see inset ii). The link between the sample deformation and the measured change in PEE pressures shows elastic stress transfer as a result of a propagating fracture.

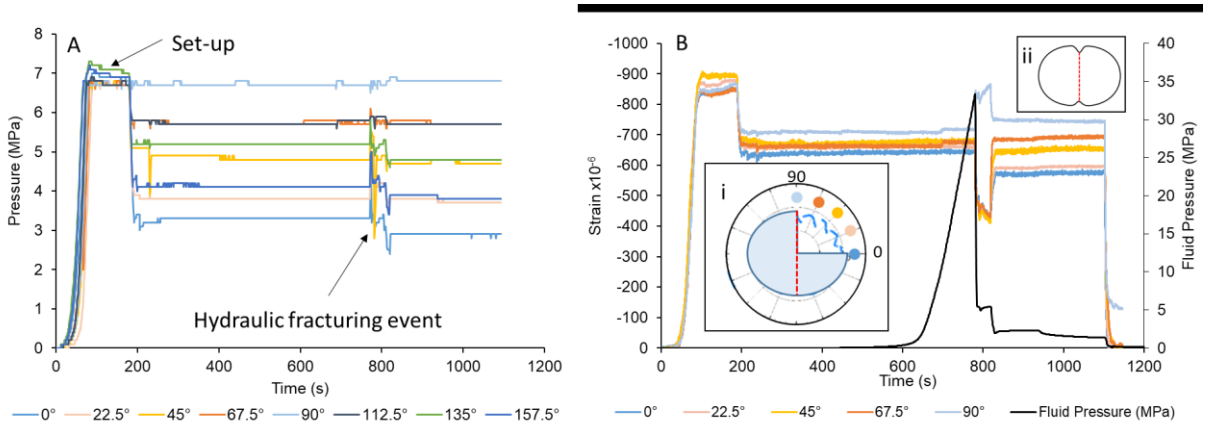

Figure 5: Experimental data for the uniform resin hydraulic fracturing test; (A) Applied experimental PEE pressures and (B) fluid injection pressure and circumferential strain at the PEEs between 0-90°.The inset shows the location of the strain data presented in B colour-coded with dark blue parallel to σ_3 and light blue parallel to σ_2. Note the strain is micro-strain and is also negative upwards on the y-axis i.e. shows contraction as the PEE pressure increases.

Water is injected at a rate of 0.01667 ml.s^{-1} (1 ml.min^{-1}) into the central bore until a hydraulic fracture initiates at a breakdown pressure of 33.36 MPa, occurring after 445 seconds of injection (781 seconds of total experiment time). The post-experiment fracture trace reveals that a fracture propagates the full length and width of the sample (Figure 6A-C). However, the surface fracture trace on the side of the sample parallel to σ_2 (at 90° in Figure 6) is not continuous – 'the fracture' is actually two separate fractures that are connected by a lateral jog within the sample, providing evidence of complex fracture propagation (Figure 6A).

Figure 6D-E presents the fluid pressure data during the test. Following breakdown (labelled G), the fluid pressure drops rapidly to 5.69 MPa over 4 seconds, before plateauing for 6 seconds at 5.40 MPa. This is followed by a further drop to 4.94 MPa over 4 seconds before the fluid pressure gradually rises to 5.28 over the next 8 seconds. The fluid pressure plateaus for a second time for 4 seconds, then gradually rises to 5.43 MPa after 8 further seconds before plateauing for a third time at 5.43 MPa. There follows a third plateau for 5 seconds. During this time, no fluid is observed exiting from the cell. A total of 39 seconds after the initial fracture propagation, the fluid pressure drops from 5.44 MPa to 2.12 MPa over 9 seconds before recovering and stabilising at 2.90 MPa +/- 0.1 MPa until fluid injection ceases. It is after this final pressure drop that fluid is observed exiting the cell through the basal fluid port, indicating a fully-connected flow path from inlet to outlet. Figure 6D shows the fluid pressure during the fracturing process, including a zoomed-in section of the pressure fluctuations described here following fracture initiation (Figure 6E). These pressure changes imply that this fracture propagates in a series of small events of varying magnitude – the first propagation leads to the greatest change in strain and largest fluid pressure drop while subsequent propagation events produce further small strain changes. This interpretation is corroborated by the strain data and is similar to that presented in recent studies e.g. Benson et al., (2020) and Gehne et al., (2019). The strain data are collected sufficient frequency (8 Hz) to capture the mechanical response on the exterior of the sample during these fluctuating fluid pressure stages, but not during the rapid fracture propagation events that are inferred to occur from the pressure transients. Here we present the circumferential strain as radar plot strain maps, which may be interpreted as a plan-view of the shape of the sample at the height at which the fibre is attached.

From the strain data it is possible to identify each stage of the hydraulic fracture propagation that is indicated by the fluid pressure results. The strain data reveal three significant propagation events – the initial propagation at 781 seconds (marked G on Figure 6D), the

562 second propagation that causes the pressure drop at 791 seconds (H on Figure 6E), and the
563 final propagation at 820 seconds that creates a fully connected flow path, and allows the
564 sample to be compressed towards its un-fractured size as the fluid pressure within the fracture
565 void drops (I on Figure 6E). We present the strain data of the intact sample (Figure 6F),
566 during each of the three main propagation steps (Figure 6G-I), and after final breakthrough
567 (Figure 6J).

568 The approximate trace of the fracture(s) at the level of the fibre optic sensor is shown by the
569 red dotted lines in Figure 6I & J only i.e. once the fracture propagation is complete.
570 Interspersed between the larger propagation events, smaller events are recorded in the strain
571 that correspond to the plateaus in the fluid pressure data e.g. at 803 seconds and 815 seconds.
572 This suggests that the fracture was propagating in small, stable steps at these times, such that
573 the newly created volume did not lead to a pressure drop i.e. the new volume was rapidly
574 infiltrated by fluid at a rate that kept up with volume creation.

575 In addition, the strain data highlight that the main propagation events resulted in different
576 amounts of displacement on the fracture plane. The initial fracture propagation at 781
577 seconds leads to approximately symmetrical strain around the plane of the fracture (90° -
578 270°) with a slight dextral offset (Figure 6G). However, the second event after 791 seconds
579 leads to appreciable dextral offset, as recorded at the axial mid-point of the sample (Figure
580 6H). The strain data show increased circumferential contraction around the vicinity of the
581 fracture trace and relative elongation elsewhere. Following the final breakthrough, the sample
582 is compressed almost back to its original shape, but a small permanent dextral displacement
583 remains.

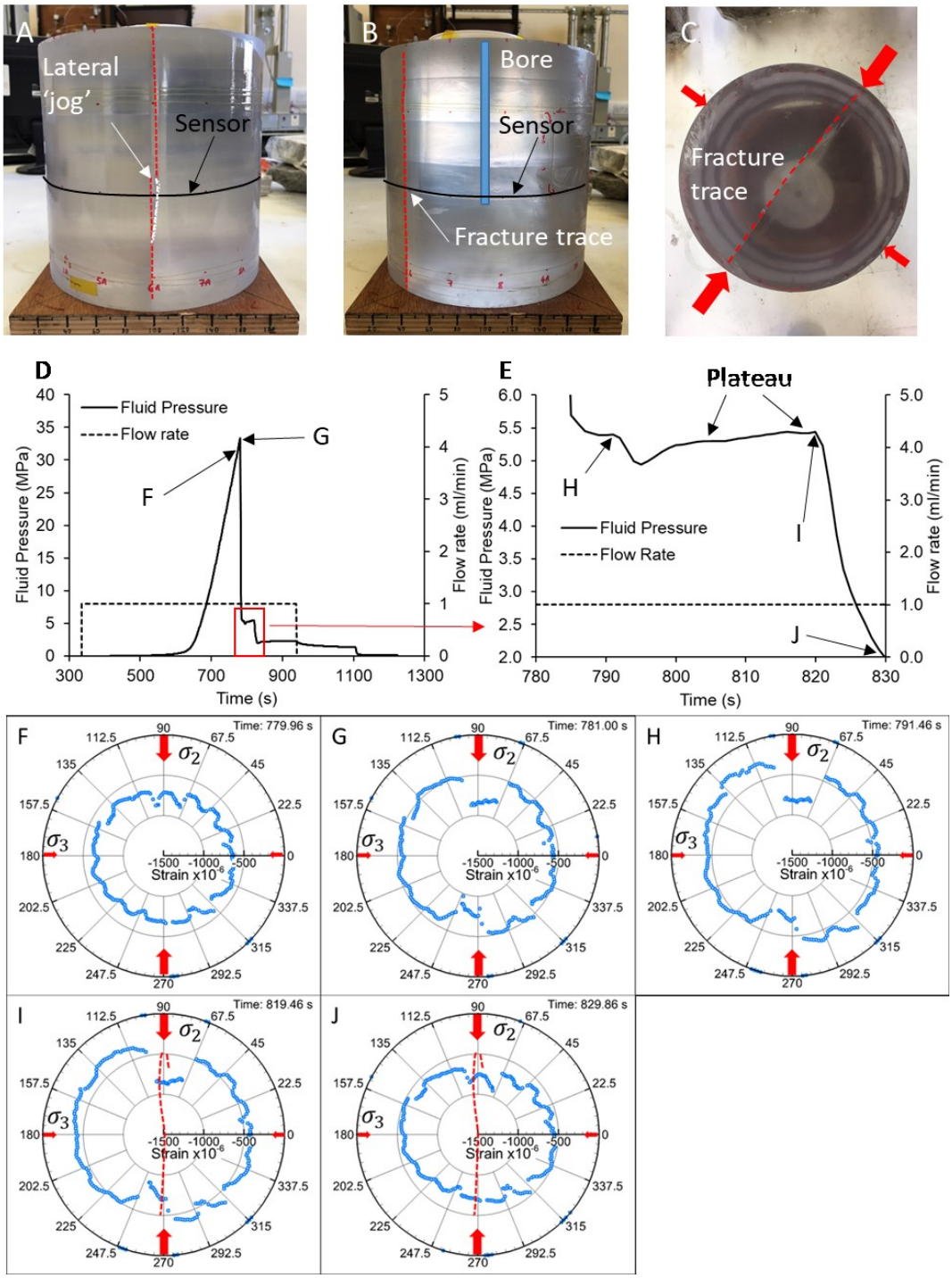

Figure 6: Fracture geometry and temporal evolution of strain and fluid pressure in the uniform resin sample. A-C) The hydraulic fracture generated in the uniform resin sample showing the lateral jog (white dotted line shows how the fractures join within the body of the sample), the full lateral and vertical extent of the fracture, and the fracture trace on the base of the sample with respect to the radial stress field. D) shows the fluid pressure results for the whole experiment and E) shows a zoomed in section highlighting the episodic fracture propagation which is correlated to the circumferential strain data. F) Circumferential strain results from the axial mid-point of the sample are shown for the intact sample, G) the first fracture event, H) the second event causing increased dextral shear offset, I) the final breakthrough event, and J) the post-fracture state once a fully connected flow path is established. The red arrows indicate the orientation of the principal stresses. Two fractures are shown by the dotted red lines because the fibre intersects both parts of the fracture that is connected by the lateral jog shown in A.

596 ### 3.1.2. Heterogeneous Resin Sample

597 Results from hydraulic fracturing of the heterogeneous resin indicate a single fracturing event
598 leading to a laterally contained fracture propagating parallel with the intermediate principal
599 stress. The presence of the included heterogeneity, striking parallel to σ_3, appears to impact
600 the final fracture geometry.

601 In the heterogeneous resin sample, fluid is injected into the central bore at 0.00167 ml.s^{-1} (0.1
602 ml.min^{-1}; an order of magnitude lower than in the uniform resin), generating an asymmetric
603 vertical bi-wing fracture that extends the full length of the sample but not the full width
604 (maximum width is approximately 160 mm, Figure 7A, B, C). The fracture initiates in the top
605 35 mm of the borehole with its trace at a bearing of 21° +/- 2° from σ_2 before rotating to
606 propagate parallel to σ_2 (Figure 7A, B). The fracture then propagates the full height of the
607 sample, such that only the top 35 mm of the fracture actually intersects the borehole (Figure
608 7A). The horizontal stress field is oriented such that a tensile fracture propagating parallel
609 with σ_2 would intersect the inclined plane at 90° (as viewed along the sample axis). The trace
610 of the fracture at the base of the sample indicates that, even at this high intersection angle, the
611 inclined discontinuity hinders the propagation, producing an asymmetrical fracture trace on
612 the base (Figure 7C). Figure 7D shows the position of the horizontal and inclined planes in
613 relation to the generated fracture. The inclined plane is depicted by the area between the
614 white dotted line and the blue outline. The white dotted line represents the location of the
615 inclined plane in line with the fracture strike. It can be seen that the estimated fracture extent
616 within the sample (red line) does not reach the inclined plane near the top of the sample, is
617 arrested along the inclined plane for a portion of its height, but propagates through the
618 inclined plane near the base.

619 There was a small leak at the injection pump during the experiment, but after tightening
620 fittings, fluid pressure follows a steep rise until fracture propagation at a breakdown pressure
621 of 37.45 MPa and subsequent pressure drop to 3.42 MPa – just above the minimum principal
622 stress of 3.20 MPa (Figure 7E). Both the fluid pressure and the strain data indicate that the
623 fracture propagation did not follow the same episodic pattern as with the uniform sample, and
624 instead, the fracture formed in a single event that lasted approximately 0.12 s. Due to the loss
625 in data, caused by poor quality signals in the fibre throughout the experiment, the equivalent
626 plot to Figure 5 has not been included.

627 Figure 7 F-J shows the circumferential strain at the intact state immediately before fracturing
628 (F), followed by the fracture propagation process over 0.12 s (G-I), and then after fracture
629 propagation once the strain has stabilised (J). Although there is some data loss caused by poor
630 signal quality, it is possible to see that the propagating fracture causes relative elongation of
631 the sample margin, normal to the propagating fracture, and contraction on the boundaries
632 parallel to the fracture. Following the onset of steady state flow, the relative circumferential
633 strain relaxes close to the original un-fractured state, although a small permanent strain
634 remains (J).

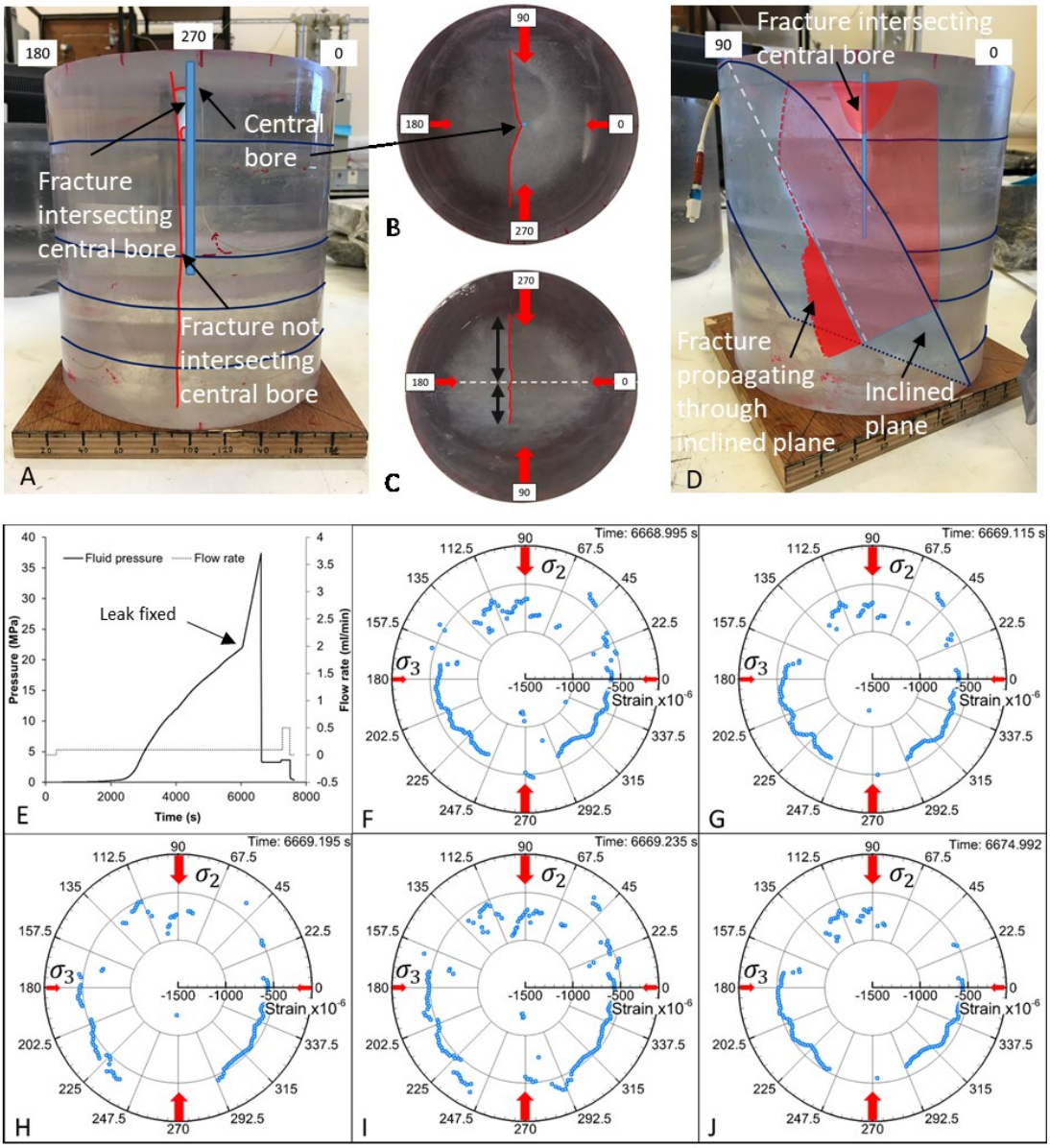

Figure 7: Fracture geometry and temporal evolution of strain and fluid pressure in the heterogeneous resin hydraulic fracturing experiment; A) Sample image parallel to the fracture showing the generated fracture intersects only the top 35 mm of the borehole. B) Top down view of the surface fracture trace showing the fracture propagated at an angle to the intermediate principal stress before rotating round to parallel. C) A base up view of the fracture trace (red) showing it is parallel to the intermediate principal stress but asymmetric (black arrows) as it is hindered by the inclined plane (dotted white line). D) A view 45° to the fracture plane showing the inclined plane in blue and the approximate extent of the fracture in red. Angles shown in A-D refer to those in the strain maps. E) Injection fluid pressure and flow rate, including the point at which a leak was tightened. Although there is some data loss throughout the experiment due to poor quality signals F) shows circumferential strain immediately prior to hydraulic fracturing. G-I) capture the propagation of the hydraulic fracturing with elongation either side of the propagating fracture at 247.5° and 292.5°, and contraction at *c.*100-105°. J) shows the post-fracture state of the sample.

3.1.3 Greywacke Sample

In this section we present the results of the hydraulic fracturing of the greywacke rock sample that show different rates of hydraulic fracture propagation and the complex interaction between fracture deformation and further propagation. The results also show dextral shear

displacements as a result of the fracture orientation with respect to the intermediate principal stress, as well as a characteristic strain pattern during hydraulic fracture propagation.

Fluid is injected into the central bore at a rate of 0.01667 ml.s^{-1} (1 ml.min^{-1} as in the uniform resin). An axis-parallel fracture is generated, propagating towards both the ends and sides of the sample and transecting the entire length of the borehole, creating a connected flow path from injection point to the cell exit. The fracture intersects the top of the sample only to one side of the central bore, but post-experiment examination and the strain data reveal that the fracture is bilateral over almost all of its vertical extent (Figure 8C-E).

Figure 8 shows the applied PEE pressures (A) and the corresponding strain (B) in the quadrant between 135° and 225° (see Figure 9), on either side of the fracture plane (which strikes approximately 172°-348°), during both the set-up phase, and during the hydraulic fracturing phase of the experiment. The fluid pressure is also shown in the strain plot. The sample is subjected to maximum isotropic ($\sigma_1 = \sigma_2 = \sigma_3$) loading of 20 MPa before reducing the radial components to the target experimental conditions. As is the case for the resin samples, the onset of polyaxial stress conditions, achieved by reducing the pressure in certain PEEs, reduces the mean stress and leads to an elongation of the sample exterior. The hydraulic fracturing process causes incremental elongations, and creates permanent deformation, especially at 180°, closest to the fracture strike (see positive elongation strain at 180° (purple) in Figure 8B). There is also a short-lived pressure spike in the PEEs in response to the initial hydraulic fracturing event (before the pressure generators automatically adjusted), that is greatest at those PEEs with lowest pressure, i.e. along the σ_3 direction.

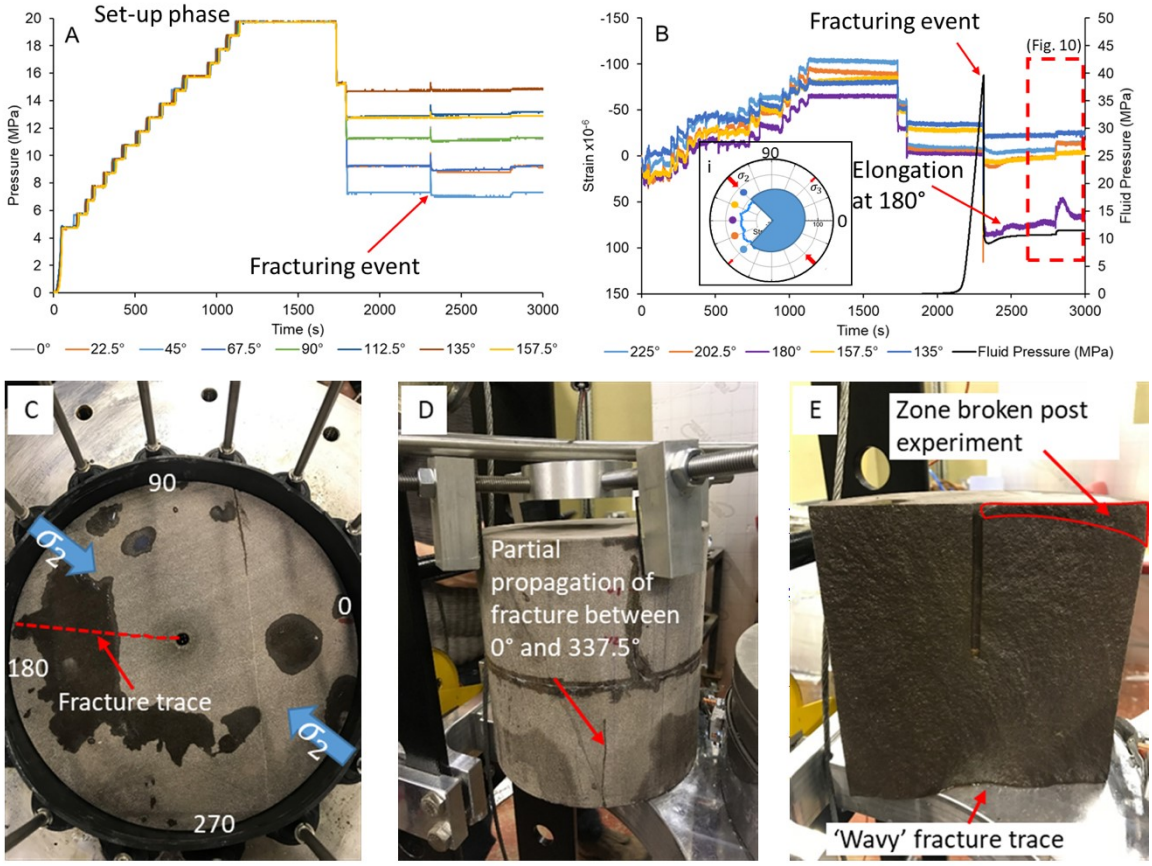

Figure 8: Experimental data and post-experiment images of the greywacke hydraulic fracture; A) PEE pressures during the set-up and hydraulic fracturing stage. B) Circumferential strain recorded at selected PEEs (between 135° and 225° in Figure

9) plotted alongside experimental fluid injection pressure. The red-dashed box shows the data presented in **Figure 10**. C) Top surface of the sample after the experiment whosing the orientation of the fracture trace to the intermediate principal stress. There is also apparent infiltration of the prexisting fracture (top right) but it is not possible to ascertain whether this was during or post experiment. D) shows the wetted fracture between 0 and 337.5 intersects the sample edge part-way up. E) shows the fracture surface after the final connected part was later broken, revealing a 'wavy' fracture trace at the sample base.

The fluid-injection pressure data (Figure 9) indicate a rapid increase until a breakdown pressure of 39.62 MPa at 2312 seconds (402 seconds after the start of injection), followed by a rapid drop to 10.54 MPa over a period of 6 seconds. A further gradual drop in fluid pressure to 9.14 MPa occurs over the next 27 seconds before the pressure rises to 10.72 MPa over the following 456 seconds. No fluid flow is observed coming out of the cell at this point (suggesting the fracture has not reached the base of the sample). The flow rate is increased to 0.08333 $ml.s^{-1}$ (5 $ml.min^{-1}$) after this time. This is accompanied by a small rise in fluid injection pressure to 11.50 MPa +/- 0.04 MPa at which point flow is observed at the cell outlet port almost immediately. It may be inferred that the increased flow rate, and the resulting increase of injection pressure, provoked a final propagation of the fracture creating the fully connected flow path.

Figure 9 shows the strain of the intact sample loaded to the pre-injection state (A) followed by the strains during the steps of fracture growth (note the times on the upper corner of each plot B-F). The direction of σ_2 is 135-315°, while σ_3 is 45-225°. This figure firstly illustrates that initial fracture propagation occurs predominantly in the direction of 172°, at a strike angle of approximately 36.5° to σ_2 over a period of 0.12 seconds. The first stage of propagation involves a near-uniform elongation of the sample circumference (C), followed by further elongation focussed around 157.5° and 207.5° (D), with comparatively little elongation around the final fracture location. Once the fracture propagates to the edge of the sample, the elongation strains around 157.5° and 207.5° relax, and the elongations are localised at the fracture strike direction (E). It is interesting to note that the differential magnitudes of the intermediate and minimum principal stresses influence the strain pattern developed (D) as more elongation is observed towards 202.5° (closer to σ_3) than 157.5° (closer to σ_2).

The strain data in D capture the configuration of strain in the sample as a fracture is propagating within it i.e. the fracture is growing but has not yet reached the sample edge. Using this pattern of strain evolution as a proxy for identifying a propagating fracture, we can see that the fracture initially only propagates towards *c.*172° (D), but once the fracture is fully formed in this direction, it begins to propagate in the opposite direction (note the configuration of the strain in E around 348°). This strain pattern then continues with increasing elongation as the experiment continues to the point shown in F 692 seconds later (which includes the flow rate increase to 0.08333 $ml.s^{-1}$ (5 $ml.min^{-1}$)), where the fracture has not propagated to the sample edge at the elevation at which the strain is measured. This implies a significantly slower rate of fracture growth than the initial hydraulic fracture. Immediately following point F, a hydraulic flow test involving stress rotations that further propagated the fracture to produce the fracture trace in Figure 8C was conducted.

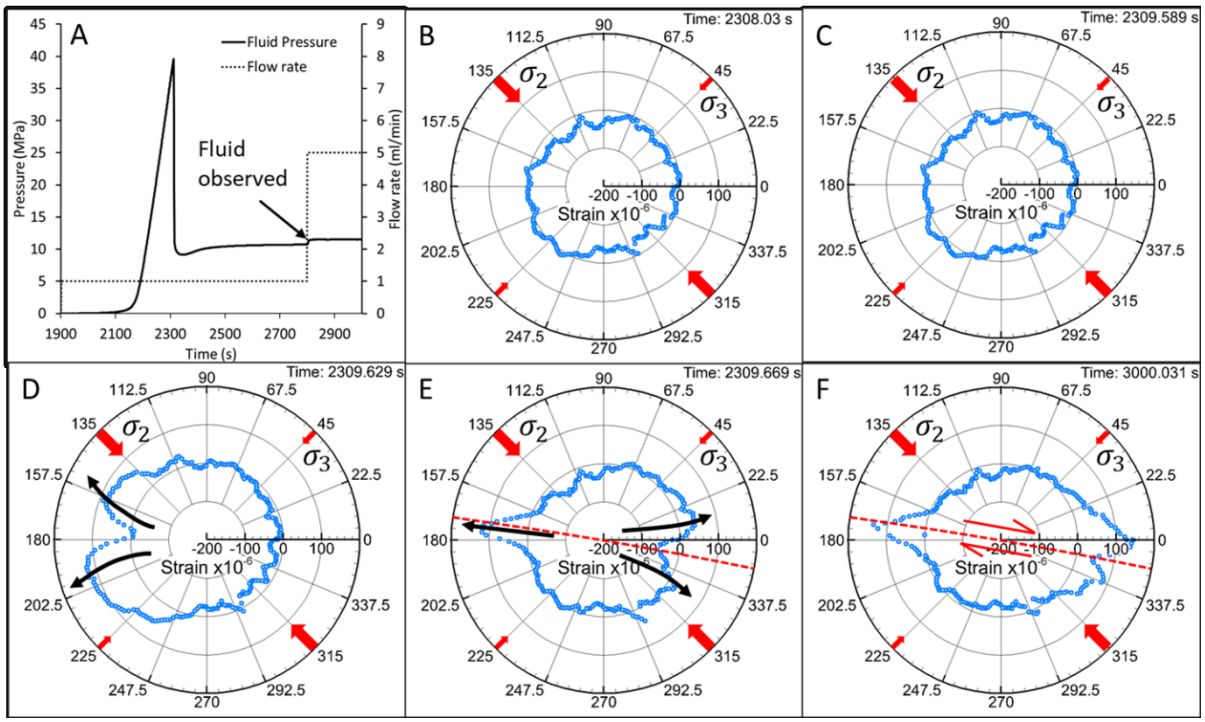

Figure 9: Fluid pressure and temporal evolution of circumferential strain in the greywacke hydraulic fracturing experiment; A) Injection fluid pressure and flow rate from the start of injection (1900 s) to end of the experimental stage (3000 s). B) Circumferential strain immediately prior to hydraulic fracture propagation indicating deformation associated with the polyaxial stress field (indicated by the red arrows). C-E) Circumferential strain maps at 0.04 s intervals during the rapid hydraulic fracturing propagation towards *c.*172°. These strain maps highlight that the fracture forms at *c.*36.5° to the intermediate principal stress, and that the sample circumference sees elongation either side of the fracture as it propagates, but before it reaches the sample boundary. Once it has reached the sample boundary (E), the strain is localised on the fracture, and the fracture begins to propagate in the other direction (towards *c.*350°). F) Circumferential strain at the end of this stage of the experiment (3000 s) indicates a gradual propagation towards *c.*350° and a dextral offset.

Figure 8 indicates that the fluid flow rate and pressure increase is accompanied by a strain response that suggests transient partial closure of the fracture in the vicinity of 180°. A closer inspection of the strain at 180° and 157.5° and the corresponding strain on the opposing side of the sample (0° and 337.5°) is shown in Figure 10 along with a sequence of schematic diagrams of our interpretation of the strain data during this transient phase. The strain and fluid pressure evolution are very gradual during the lower flow rate conditions (Figure 10 Point 1) before the changes induced by the increased fluid flow rate. At the onset of higher flow rate (Point 2), strain at 180° shows a contraction, which is interpreted as fracture closure, followed by an elongation until the fluid pressure rise begins to stabilise (Point 3). This expansion is also observed in the strain at 0° and 337.5° suggesting a small amount of fracture propagation. At this point fluid is observed exiting the cell, so it is possible that this is the event that fully connects the inlet with the outlet. When the fluid pressure stabilises, the strain at 0° and 337.5° also stabilises, but the relative contraction continues in the direction of 180° (Point 4). This trend continues until approximately 2850 seconds of overall experiment time, before an initially gradual and then more rapid expansion occurs in the direction of 0° and 337.5°. As this propagation proceeds, the strain in the direction of 180° stabilises to a new equilibrium (Point 5). This can be interpreted as the fracture closing in the direction of 180° (where it has propagated to the sample edge) and then propagating in the opposite direction and at a much slower rate. Furthermore, fracture propagation continues to the end of this stage of the test even though fluid pressure remains relatively stable. These mechanisms of the fracture-propagation process permit an inference that there are significant interplays occurring between the fluid injection, fracture opening/closing and propagation, and

752 modifications of the interior strains (inferred because of the exterior strains, but not measured
753 here). The observations point to an evolution that is non-monotonic.

754

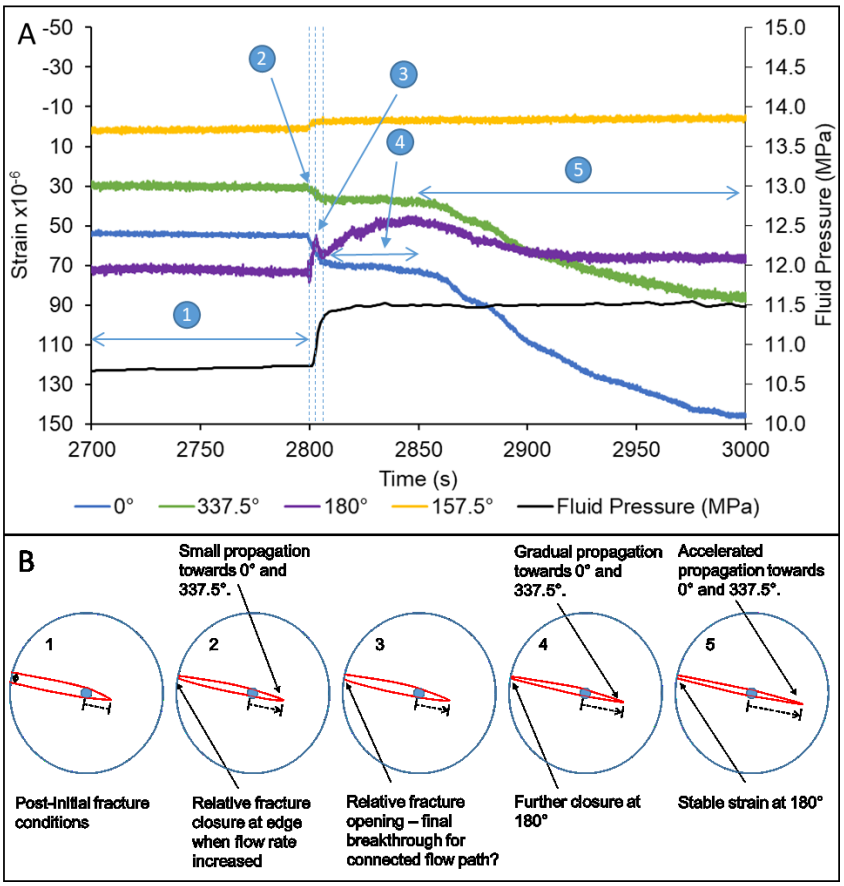

755

756 **Figure 10:** Close up view of the non-monotonic relationship between injection fluid pressure and transient strain data in the
757 greywacke sample and associated interpretation; A) shows the increase in fluid pressure and the transient strain behaviour
758 (from the dashed red box in Figure 8). B) A not-to-scale schematic interpretation of the strain data showing the propagation
759 of the fracture during this transient phase at each labelled point in A. Point 1 shows the stable conditions at 1 ml/min flow
760 rate. Point 2 shows that the flow rate increase from 1ml/min to 5 ml/min causes relative fracture closure towards 157.5° and
761 180° but relative fracture opening towards 0° to 337.5°. Point 3 shows a relative fracture opening at 180° that may indicate
762 final breakthrough as this coincides with observed fluid flow. Point 4 indicates further closure at 180° but stable strain at 0°
763 and 337.5°. From Point 4-5 relative fracture opening towards 0° and 337.5° increases gradually before accelerating after
764 approximately 2850 s, while deformation stabilises in the direction of 157.5° and 180° after 2900 s. This is interpreted as a
765 change in locus of the fracture propagation towards 0° and 337.5°.

766 **4. Interpreted fracture flow behaviour in response to fluid pressure and stress**
767 Here we analyse the flow test results within the framework of the parallel plate model and
768 modelled stress field. We show the impact of fluid pressure and normal and shear stresses on
769 fracture flow in each of the three fractured samples. Results indicate that normal stress has a
770 first order control on fracture permeability, but that shear displacement at fracture
771 orientations of maximum shear exerts a secondary control. Furthermore, in the greywacke,
772 the direction of shear is important in controlling the fracture permeability.

773 The unique design of the GREAT cell allows a rotational change of the radial stresses during
774 an experiment (McDermott et al., 2018). This capability has been employed to investigate the
775 effect of apparent fracture-normal stress on the fluid flow within the fracture in each sample.
776 Here, we describe how we calculate an effective fracture permeability to compare between
777 different samples and loadings. The effective fracture permeability is calculated using the

parallel plate model of the cubic law (Zimmerman & Bodvarsson, 1996) that relates volumetric flow to the pressure gradient along the fracture length, and the fracture aperture:

$$1)\quad Q = \frac{wb^3}{12\mu}\frac{\Delta P}{L}$$

where Q is the volumetric flow rate (m^3/s), w is the fracture width (m) viewed along the sample axis, b is the fracture aperture (m), μ is the dynamic viscosity of the fluid assumed in each case to be 0.00103 Pa.s, P is the fluid pressure (Pa), and L is the fracture length in the direction of the flow (m). During the flow period we have no independent measure of fracture aperture (b), so this parameter is the calculated unknown. For the greywacke and the uniform resin samples the length L is taken as the distance between the base of the borehole and the base of the sample, and the width w is taken as the sample diameter, since the fractures intersect the full borehole length and extend for the full sample width. An estimated length of 0.165 m and width of 0.16 m is taken for the heterogeneous resin sample where the fracture intersects the borehole for the top 35 mm and does not propagate to the sample sides. We adopt the parallel-plate model to facilitate comparisons between different experimental deformation outcomes and different mechanical loadings, even though it assumes that the aperture (b) is constant across the fracture width, which cannot be true in the case of a contained fracture (heterogeneous resin), and is also unlikely to be true in the homogeneous resin. Thus, the values calculated here are suitable for comparisons only.

Permeability calculations are performed on fluid flow data only after the fracture reaches its full extent. However, in the case of the greywacke the fracture continues to propagate during the fluid flow part of the test, so it is not possible to calculate a representative permeability during this phase as we do not know the fracture extent. Consequently, we present differential pressure (ΔP), determined as the difference between the upstream pressure and downstream pressure. Equation 1 can be rearranged to determine the effective hydraulic aperture:

$$2)\quad b = \sqrt[3]{\frac{12\mu QL}{\Delta P w}}$$

Assuming there is no contribution from the un-fractured material to fluid flow, the effective permeability of the fracture is then given by (Witherspoon et al., 1980; Zimmerman & Main, 2003; Zimmerman & Bodvarsson, 1996):

$$3)\quad k = \frac{b^2}{12}$$

Fluid exits the cell (after flowing through the fractured sample) through a central fluid port in the base platen (which also has a gathering plate), meaning the resultant calculated permeability constitutes the average for the entire fracture. Apparent normal stress (σ_n) and shear stress (τ) acting on the fracture is calculated from the orientation of the fracture with respect to the nominal experimental state i.e. the applied far-field stress state:

$$4)\quad \sigma_n = l^2\sigma_1 + m^2\sigma_2 + n^2\sigma_3$$

$$5)\quad \tau = \sqrt{[(l^2\sigma_1^2 + m^2\sigma_2^2 + n^2\sigma_3^2) - \sigma_n^2]}$$

where l, m, n are directional cosines for the normal vector of the fracture plane relative to the direction of the principal stresses.

Linear elastic numerical modelling of the stress conditions that are generated by the GREAT cell (Figure 3) show the generated fracture is likely to have a complex stress field along its length as a result of the non-uniform polyaxial stress field. To address this in our analysis of the stress influence on fluid flow, we model the stresses on a hypothetical plane representing the generated fracture with an angular offset from σ_2 corresponding to the stress rotations. These results indicate that for each orientation there may be a gradient of normal stress in the fracture, with highest stresses at and near the injection borehole. However, as a first approximation, we take the mean, integrated by area, of the numerically modelled normal and shear stresses along the hypothetical fracture from the centre to the edge.

We assume, for now, that the apparent stress state of an intact sample provides a suitable frame of reference to calculate the stress components on the fracture plane. However, this is not correct in the case of a fully open fracture void, where the stress at the fracture surface is a function of the shape of the fracture opening and the far-field stress, rather than purely the resolved far-field stress state. Nevertheless, due to the lack of internal strain measurements from within the sample, the apparent fracture normal and shear stresses in this case provide a practical tool for use in comparing experiments, and to express relationships between fracture fluid pressure and stress.

In the following sections, we present results from each sample for the two types of hydraulic flow tests described earlier, interpreted in the framework described above. These flow tests are designed to investigate the influence of apparent fracture-normal stress and fluid pressure on the fracture flow properties.

4.1. Effective fracture permeability in deforming fractures as a function of normal and shear stress

To investigate fracture permeability as a function of apparent normal stress on fractures whose surfaces are juxtaposed by varying displacements, a fracture flow test with radial stress rotation is conducted on the uniform resin sample. Because the fracture reaches the edge of this sample, the changing stress field is expected to induce a small degree of displacement between the two almost-separated blocks (though at the measurement locations for the strain sensors, the blocks are fully separated) initializing a new static configuration of the mismatched fracture surface asperities. The set-up loading procedure shown in Figure 4 is followed until the onset of polyaxial stress loading. In this experiment, the polyaxial stress is initially set up in the same orientation as that under which fracturing is induced in the previous fracture test, before subsequently rotating the radial stress field by 90° and then rotating the stresses anti-clockwise by the angular spacing of the PEE (22.5° each PEE) in relation to the original stress field orientation (see stress arrows on strain maps, Figure 11). Water is injected into the central bore at a constant rate of 0.41667 $ml.s^{-1}$ (25 $ml.min^{-1}$) and a downstream pressure of 3.45 MPa (500 psi) is applied from the start of the polyaxial loading phase (i.e. before the stress rotations). In order to achieve this high downstream pressure, the radial stresses were raised each by 1 MPa over the original stress conditions (see Section 2.3).

Circumferential strain maps for each rotational stage are presented in Figure 11. These are absolute values of circumferential strain differenced from the start of the radial confinement (not incremental circumferential strains). As the stress field rotates (from plot A to C) there is an increase in apparent dextral shear displacement. This consists of a combination of the elastic deformation of the block in response to the changing stress orientation, which causes an elongation of the circumference in the direction of the minimum principal stress, as well as dextral shear that separates the blocks where the fracture intersects the sample margin (and presumably also within). Plots D and E show an apparent reduction in the displacement or

reversal of the displacement direction. In plot D, this is caused primarily by the elastic deformation of the fractured blocks as the stress parallel to the fracture increases, while in plot E this process is in addition to a partial reversal in displacement. Physical and visual analysis of the sample (once recovered from the cell) reveals that where the fracture intersects the vertical edges of the sample it is possible to feel the dextral displacement of the two almost-separated blocks.

Using equations 1-3, effective fracture permeability is calculated and plotted against apparent fracture-normal stress (Figure 11). The displacement of the two fracture surfaces during the stress rotations alters the simple relationship between the apparent fracture-normal stress and effective fracture permeability (Figure 11). Nevertheless, an increase in apparent fracture normal stress leads to a decrease in effective fracture permeability despite the difference in displacement on the fracture, suggesting that normal stress has the first order control over the fracture permeability. A simple power law trend between results for stress orientations B, C, E, and F in Figure 11 returns a correlation coefficient (r^2) value of 0.9997, suggesting a strong relationship between the apparent fracture-normal stress and effective fracture permeability. However, at the stress field orientation where the fracture is closest to being critically stressed with respect to σ_2 i.e. when shear stress is greatest (2 MPa) and dextral shear displacement is largest (D), calculated effective permeability is higher than predicted from the normal stress relationship.

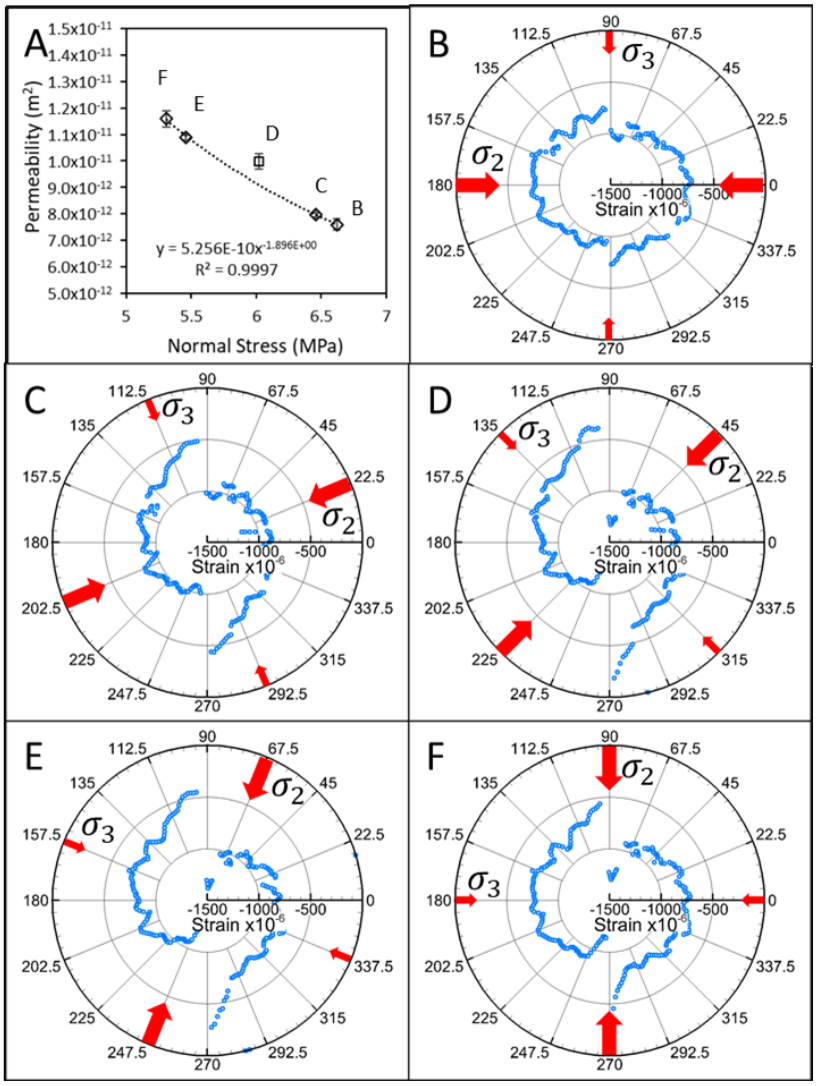

Figure 11: Permeability and circumferential strain data during radial stress rotations in the uniform resin; A) Permeability vs. normal stress during a rotation of the horizontal stress field in the uniform sample. Error bars are one standard deviation from the mean permeability for each stage. B-F) Strain maps for each stage corresponding to the labels in panel A, highlight the shear offset during horizontal stress rotation. Shear offset is largest when the fracture is 45° to σ_2 i.e. largest theoretical shear stress (D).

Figure 12 presents further evidence for the influence of shear displacement on the fracture permeability in the fracture fluid flow results for the greywacke. This test immediately follows the fracturing stages described in Section 3.1.3 and involves the same stress rotation protocol as for the uniform resin i.e. through 90° in 22.5° steps before reverting back to the fracturing stress field. The strain data show the continued growth of the fracture from Figure 12A until Figure 12C in the direction of 350° when it appears to be fully formed. During these stages the circumferential strain data suggest dextral shear displacement. During Figure 12D the strain data no longer show the characteristic shape of a propagating fracture and, at this time, the orientation of the intermediate principal stress to the position that the initial fracture propagation reaches the sample boundary (170°) is greater than 90°. This means that the stress field is now trying to shear the sample in a sinistral fashion, where previously it was dextral. Furthermore, the strain in Figure 12E shows a clear sinistral offset in the vicinity of 350° indicating that the fracture experiences sinistral shear displacement before the stress reverts to the original stress field orientation in Figure 12F.

Figure 12G and H also show plots of the mean differential pressure (+/- 1 standard deviation) during each stress field rotation. Here we choose to present differential pressure (rather than permeability as in previous analyses) because the calculation of permeability using equations 1-3 requires the width and length of the fracture to be known. In this case, as the fracture is still propagating from Figure 12A-C we cannot know these parameters. The two plots indicate that, even though the fracture continues to propagate during these stages, when the stress fields are approximately the same during Figure 12A and F, the differential pressures are essentially equal. This indicates that the dominant flow path is unaffected by the fracture propagation and that this may be due to the location of our strain sensors at the axial mid-point of the sample.

The stages shown by Figure 12B and E have similar magnitudes of normal and shear stresses on the fracture but the strain measurements indicate that the shear displacement is in opposing directions. As the differential fluid pressures in stages A and F are comparable, we can infer that the continued fracture growth occurring in stages shown by Figure 12A-C does not influence the fluid pressure, possibly because the dominant flow path is already created prior to these stages. Using this assumption, we can compare the differential fluid pressure in stage B during dextral shear displacement with that of stage E and sinistral shear. Even though the shear stresses and normal stresses are similar, differential pressure during dextral shear is 4.83 MPa lower than during sinistral shear displacement. This suggests that the fracture surface geometry (see the wavy profile at the sample base and the rough fracture surface in Figure 8E) influences the effective hydraulic aperture. Therefore, we infer that the difference in differential pressures at similar normal and shear stresses in stages B and E are as a result of the different motions of shear displacement on a rough and wavy fracture surface.

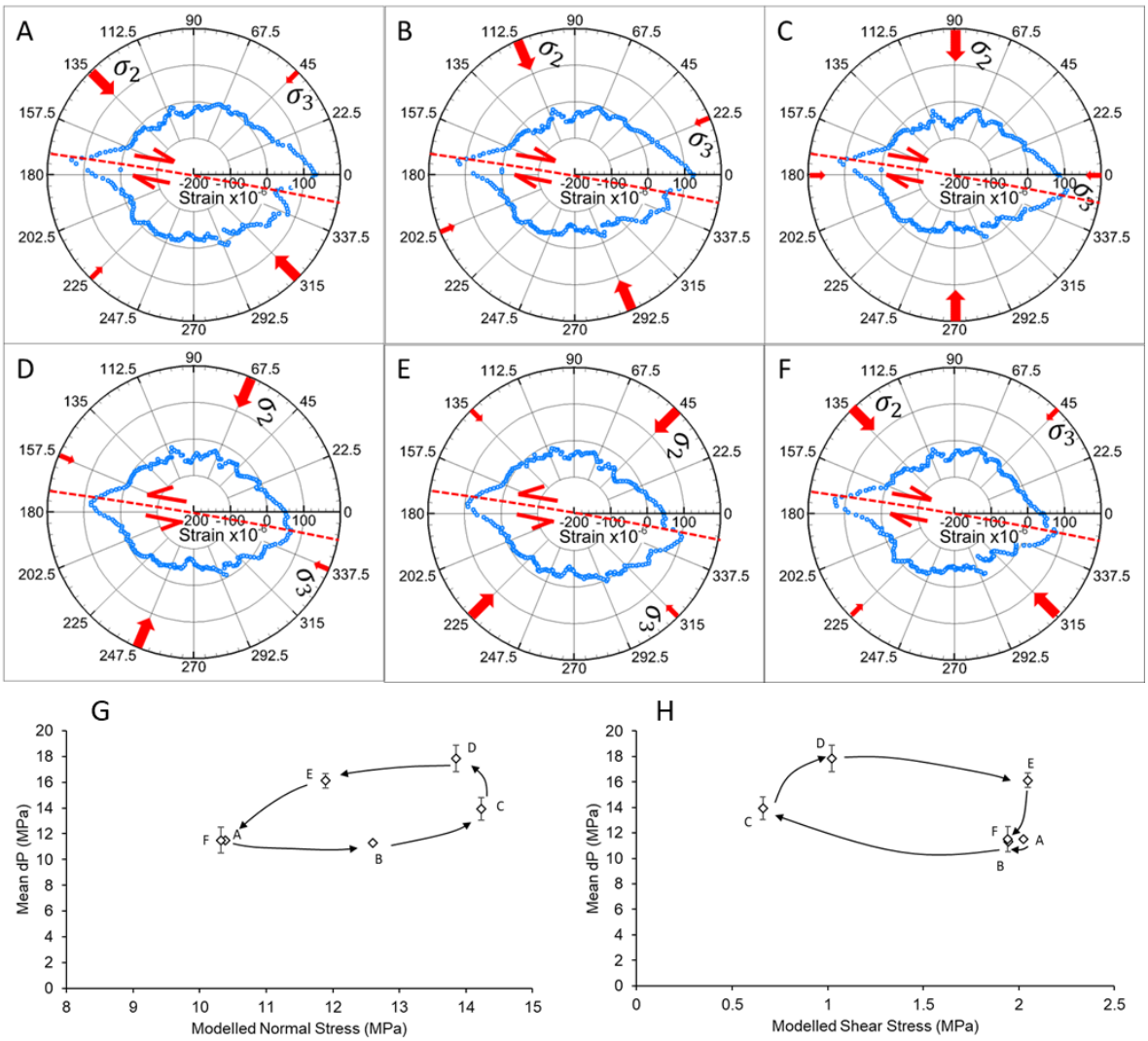

Figure 12: Circumferential strain data and differential fluid pressure relationship with normal and shear stress during stress field rotation in the greywacke sample; A-C) Circumferential strain data during radial stress field orientation (shown by the red arrows) indicates the continuation of the slow fracture propagation towards 350° and the dextral shear offset. D-E) Circumferential strain data suggest the reversal of the shear offset orientation to sinistral. F) A return to the same stress field orientation as A showing the reinstatement of dextral offset. The strain at 350° indicates the fracture has propagated fully at the horizon of the strain sensor. G) shows the relationship between the differential pressure and modelled normal stress on the fracture, and H) the relationship between differential pressure and modelled shear stress. Differential pressure is significantly higher when shear offset is sinistral (D and E) suggesting that the sense of shear offset is an important factor controlling fracture fluid flow.

4.2. Effective fracture permeability as a function of fracture-fluid pressure

We compare calculated permeabilities between experiments conducted at different downstream fluid pressures by normalising each dataset against the permeability when the fracture is under the greatest apparent average fracture-normal stress of 6.62 MPa (stress orientation shown by the red arrows in Figure 13B). This allows comparison of the change in permeability caused by the change in normal stress induced by a rotation of the stress field under different fluid pressure conditions. To take into account the fluid pressure we calculate the ‘net fracture stress’ – a term used here to avoid confusion in terminology with ‘effective

stress' because the resin sample in these experiments is so impermeable there is no mechanism for the exchange of fluid between the fracture and the resin 'matrix'. Therefore, the fluid pressure in the fracture acts as a traction boundary on the fracture surface and the net stress on the fracture surface can be calculated from the apparent average fracture-normal stress with respect to the far-field stress state (σ_n), and the fracture-fluid pressure (P):

6) $\sigma_f = \sigma_n - P$

This formulation is selected to establish a single parameter that may be used for determining a relationship between fluid pressure and stress. In doing so, we assume that σ_n at the fracture boundary is not dependent on P or structural changes induced by variations in P.

The permeability data from four repeat tests on the heterogeneous resin sample, at different downstream pressures, are plotted in Figure 13. Circumferential strain data for all four fracture flow tests showed no variation as a result of the different fluid pressures (Figure 13B-F). For each downstream pressure, the change in average normal stress across the fracture during a full rotation of stresses is the same (1.31 MPa), however, Figure 13 shows that with reducing net fracture pressures (i.e. increasing fluid pressure) there is a larger change in permeability for a given change in normal stress.

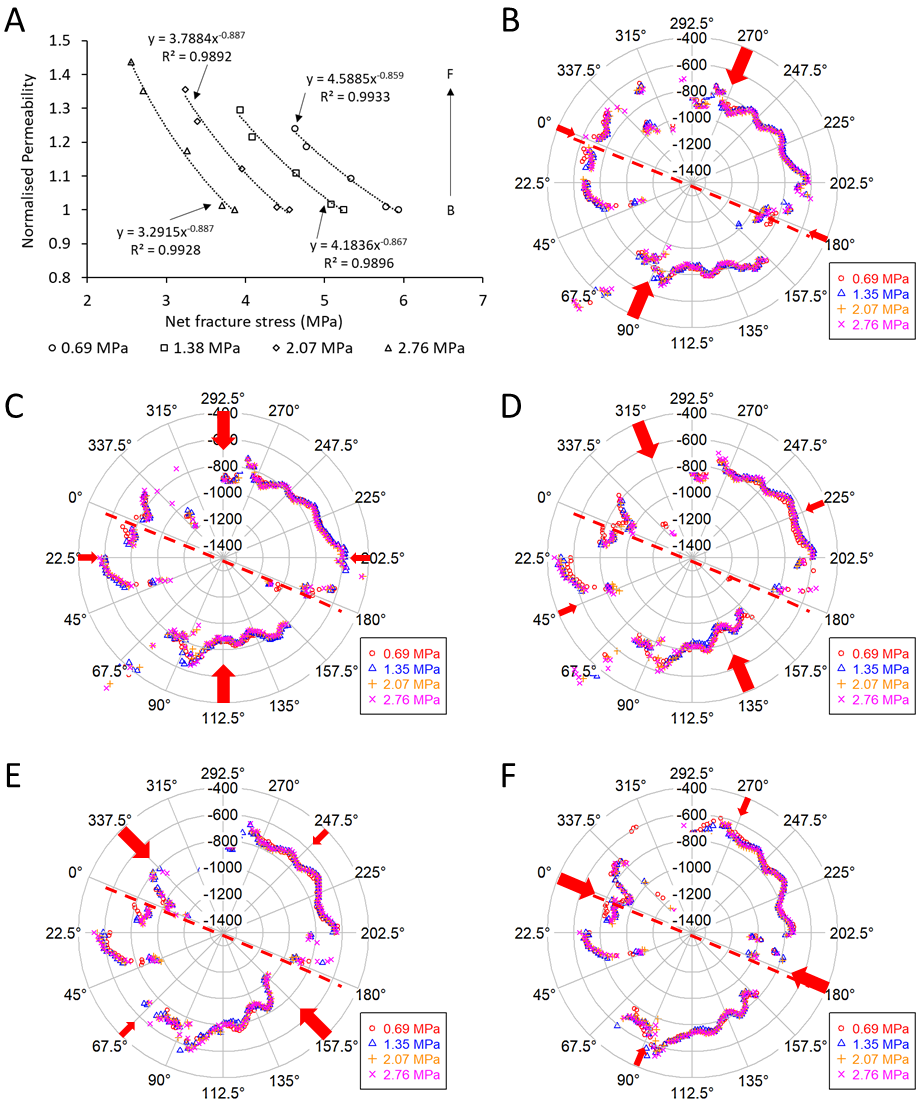

964 **Figure 13:** Normalised permeability and circumferential strain data for stress rotations at controlled downstream fluid
965 pressures; A) Normalised permeability vs net fracture stress (normal stress - downstream fluid pressure) for downstream
966 fluid pressures of 0.69 MPa, 1.38 MPa, 2.07 MPa, 2.76 MPa, B-F) Circumferential strain recorded at different stress field
967 orientations (indicated by the red arrows) for each fluid pressure. Radial axis is Strain $x10^{-6}$. At high fluid pressures (lower
968 net fracture stress) the change in permeability as a function of normal stress is larger than at low fluid pressure. The
969 approximate location of the fracture is plotted as a dashed red line and the orientation of the stresses is shown by the red
970 arrows. These data indicate that the different fluid pressures are not causing deformation around the circumference of the
971 sample and that differences in the permeability must therefore be attributed to deformation at the fracture surface.

972

973

974

5. Discussion

We describe experiments that focus on hydraulic fracturing of zero- and low-permeability samples under polyaxial stress conditions. The samples deform elastically at first in response to the applied boundary loads, and then permanently by hydraulic fracturing under constant-flow-rate water injection into a partially penetrating axial borehole. Fractures in the two resin samples form parallel with the intermediate principal stress, a response compatible with a tensile failure process, while the hydraulic fracture in the greywacke propagates at an angle striking 36.5° to the intermediate principal stress direction, compatible with the development of a primary shear fracture. The subsequent fluid flow behaviour of the fracture(s) shows dependency on several factors: absolute fluid pressure inside the fracture void, the difference in fracture-fluid pressure and the resolved far-field normal stress on the fracture plane (which is varied, as we rotate and/or alter the far-field boundary conditions), and the relationship between the fracture orientation and the intermediate far-field stress component. The set of observations provides a basis from which to examine some existing ideas concerning the controls on effective fracture apertures.

In the uniform resin sample a hydraulic fracture is formed at a breakdown pressure of 33.36 MPa under a minimum principal stress of 3.30 MPa, while in the heterogeneous resin breakdown pressure is 37.45 MPa with a minimum principal stress of 3.20 MPa. As these fractures are approximately parallel to the intermediate principal stress, the classical tensile failure model (Hubbert & Willis, 1957) suggests that the tensile strength of the sample is approximately 30-34 MPa – slightly lower than the 'typical' value provided by the polyester resin supplier of 40 MPa, but significantly higher than the Brazilian test results. There are a number of possible reasons for this. Firstly, the Brazilian test results indicate an increase in strength with decreasing equivalent diametric strain rate, suggesting that the higher breakdown pressure achieved at the lower flow rate in the heterogeneous resin is as expected for this material (but unusual for rocks). Secondly, the uniform resin hydraulically fractured after 445 seconds (approximately 7.5 minutes) which is a similar timescale to the highest strength samples in the Brazilian testing (26.5 MPa; 9 minutes, and 28 MPa; 9.5 minutes – see supplementary information), but the heterogeneous resin took far longer due to a combination of the pump leak (indicated in Figure 7E, and rectified at an injection pressure of 22 MPa) and the slower flow rate. Finally, Haimson & Zhao, (1991) and Zhuang et al., (2018) show that hydraulic breakdown pressures at the laboratory scale are dependent on the borehole size effect and pressurisation rate with smaller borehole diameters leading to higher breakdown pressures. The small diameter borehole in the greywacke (6 mm) and resins (3 mm) could also be a contributory factor in elevated breakdown pressures.

In the uniform resin sample the fracture propagates in the orientation approximately as predicted by the classical tensile failure model (Hubbert & Willis, 1957), and the strain and fluid pressure data show that the propagation behaviour is not a single event. Multiple stages of fracture propagation are observed as the fracture continues to extend towards the boundaries over a 39 second period after initiation. Three major events can be identified that correspond to fluid pressure drops (as shown in Figure 6) interspersed with smaller events that correlate with plateaus in fluid pressure. These events measured in the strain data at constant fluid pressure suggest the fluid infiltration was keeping pace with fracture propagation i.e. the fracture propagation was stable, as seen for viscous fluids (Stanchits et al., 2015; Zoback et al., 1977). The strain data show increased circumferential contraction around the vicinity of the fracture trace and relative elongation elsewhere. This pattern of strain is compatible with (but not discriminate against some alternate) an interpretation of the sample responding as two thick crescents, with a pronounced-aperture fracture opening in the centre with a closed-fracture tip near the sample margins. A small variation in the symmetry

of the boundary loads shown in Table 2 (particularly PEEs 8 and 1 that are 45° to the principal stresses) may cause the small amount of dextral shear observed during the fracturing process, which increases with each step of the propagation. This suggests that even small variations in the orientation of the developing hydraulic fracture (e.g. by local heterogeneity, or local stress changes caused by hydraulic stimulations with pre-existing fractures (Mack, 2016; Sarmadivaleh, 2012)) could lead to a component of shear displacement even in situations where pure tensile failure might be expected.

The fracture in the heterogeneous resin sample propagates out of the top 35 mm of the borehole at an angle of 21 +/- 2° to the far-field intermediate principal stress (σ_2) before aligning parallel with σ_2 (Figure 7). Both the fluid pressure and the strain data indicate that this fracture propagation occurred as a single event. This axis-parallel fracture intersects the pre-existing, axis-normal, 'horizontal' heterogeneities defining the initial 'layers' at approximately 90°, propagating through all the layers to create a fully-connected flow path from the top to the base of the sample. This response is as expected based on current understanding of fracture-interface interactions, whereby hydraulic fractures that intersect interfaces at high angles are more likely to cross the interface than to open the interface or be arrested, offset or /deflected (Chuprakov et al., 2010; Gu et al., 2012; Jamison & Azad, 2017; Meng & De Pater, 2010; Renshaw & Pollard, 1995; Sarmadivaleh & Rasouli, 2014; Sarmadivaleh, 2012). The induced fracture also intersects the inclined plane/discontinuity at a 90° difference in strike, but the asymmetrical fracture trace on the base of the sample indicates that the inclined plane/discontinuity hindered or altered fracture propagation through it. This relationship suggests that fracture-rock-interface interactions need to be considered in three dimensions to determine fully whether fracture arrest, propagation or deflection may occur at interfaces.

Breakdown pressure for the greywacke sample is 39.62 MPa with a minimum principal stress condition of 7.30 MPa. Assuming the Hubbert & Willis (1957) model of hydraulic fracturing, this would suggest a tensile strength of approximately 32 MPa - higher than that determined from Brazilian testing results (see Table 1 and supplementary information). For the greywacke, Brazilian testing did not reveal a strong rate dependence and strengths were generally consistent, suggesting that the elevated breakdown pressures may be due to the borehole size effect (Haimson & Zhao, 1991; Zhuang et al., 2018). However, as the hydraulic fracture generated in the greywacke propagates at an angle of 36.5° to the intermediate principal stress suggesting a shear component, a simple comparison of breakdown pressure and tensile strength as above is not appropriate. The circumferential strain data capture the propagation of the fracture in one direction over a period of 0.12 s and also the gradual extension of the fracture trace in the opposite direction during continued fluid injection. This is in notable contrast to the heterogeneous resin that is laterally constrained but does not continue to grow. As the fracture in the greywacke propagates outward from the central borehole, the strain data indicate that the sample circumference experiences elongation normal to the propagating fracture plane, but very little strain parallel to it. Once the fracture propagates fully to the boundary, the strain normal to the fracture recovers, suggesting an elastic deformation around the propagating fracture tip. It is not possible to deduce from this individual greywacke experiment why the fracture propagated at an angle to the intermediate principal stress, but one potential explanation may be provided by numerical simulations of borehole mechanics with different radial stress magnitudes, thus accounting for the role of σ_2. These indicate that the circular shape of the central borehole and displacement of the borehole wall promote mixed-mode and shear failure as the dominant propagation mechanism in natural materials such as Berea sandstone, and other material types with lower porosity and permeability, as a result of well pressurisation (Alruwaili, 2016, Alruwaili et al.,

2017). The temporal evolution of the strain in the vicinity of the fracture (as described in Section 3.1.3) hints at a complex interaction between fracture deformation and subsequent fracture growth.

Results from the fracture fluid flow experiments conducted on the uniform resin sample under rotating radial stress conditions show that although apparent fracture-normal stress is the main controlling factor on fracture permeability, fracture orientation with respect to the polyaxial stress field is also important, especially for vertical hydraulic fractures.

The process of shear dilation has long been recognised as a mechanism by which fracture conductivity may be increased (Barton et al., 1985; Chen et al., 2000; Ye & Ghassemi, 2018). It refers to the opening of the fracture aperture due to the displacement of two non-planar surfaces juxtaposing 'high points' against each other i.e. contacting asperities, and the surface roughness is a key component for shear stimulation leading to self-propping fractures (Ye & Ghassemi, 2018). In contrast, Rutter & Mecklenburgh (2018) provide evidence of transmissivity reduction as a result of fault slip and the generation of wear products in the fracture during dynamic failure. It should be noted that in our experiments displacement caused by the rotation of the stress field is not the same process of fracture/fault reactivation that may generate wear products, or stick-slip behaviour in frictional sliding experiments, such as those conducted by Rutter & Mecklenburgh (2018) and Ye & Ghassemi (2018). The process in our experiments is much slower and each stress orientation reflects a stable configuration of the juxtaposed fracture surfaces i.e. in a new stick-state depending on the orientation within the 3D stress field (more akin to Chen et al. (2000), Hofmann et al. (2016), and Zhou et al. (2015) who used spacers to control the magnitude of fracture surface displacement). Calculated permeability at maximum shear stress and dextral displacement (inferred from the circumferential strain data) in the uniform resin is larger than predicted from the normal stress relationship derived from the other stress orientations (Figure 11). We interpret that this is a result of the (minor) dextral offset that leads to the juxtaposition of fracture surface asperities when the fracture is oriented at maximum shear stress – approximately 45° to the intermediate principal stress. In addition, our results support the concept that shear direction is an important factor as the sinistral offset in the greywacke leads to higher differential pressures (Figure 12B vs E), which suggests that the initial dextral offset opens the fracture, but the reversal of displacement re-matches the fracture surfaces and increases differential pressure. This is in agreement with previous studies that have numerically shown a directional dependence of permeability on shear offset (Cheng et al., 2017).

These experimental results highlight that normal stress exerts first order control on fracture flow behaviour, which is in agreement with recent field data from hydraulic pumping tests in over 200,000 shallow boreholes in crystalline rock (Mattila & Follin, 2019). However, Mattila & Follin, (2019) also indicate that understanding the full 3D stress state is fundamental for predicting whether fractures will be conductive to fluid flow due to the potential for shear dilation/contraction to significantly alter fracture fluid flow characteristics. This has been discussed by Lei et al., (2017) who showed numerically the importance of the full polyaxial stress state magnitude and orientation on fracture permeability.

The response of fracture closure to a change in normal stress has been studied with a wide range of analytical and numerical approaches (Bandis et al., 1983; Barton et al., 1985; McDermott & Kolditz, 2005; Walsh et al., 2008; Wang & Sharma, 2017), many of which need stochastic or physical data for the fracture surface. A commonly used empirical approach is the Goodman (1976) model. We choose to use this as we do not have the fracture surface information required to parameterise other models. The Goodman (1976) model

calculates the change in fracture aperture (ΔV_j) as a function of the initial stress (σ_i), the normal stress (σ_n), and the maximum fracture closure (V_m), in our case fracture aperture:

$$7) \quad \Delta V_j = V_m - (V_m - \sigma_i)\frac{1}{\sigma_n}$$

Here we take the initial stress to be the net fracture pressure at the start of each stress rotation and use the same calculations for normal stress as in previous analyses. Choosing the net fracture pressure allows for the variation in fracture aperture with fluid pressure, and highlights the importance of the fluid pressure in the process. The model (dashed lines in Figure 14) is calibrated to the calculated experimental fracture aperture obtained from Equation 2 for each experiment (symbols in Figure 14) by adjusting the maximum fracture closure parameter (V_m). Figure 14 shows the best-fit model (V_m = 3.50 x10^{-3} mm) of fracture closure for each experimental downstream pressure in the heterogeneous resin sample (0.69 MPa, 1.38 MPa, 2.07 MPa, 2.76 MPa). It indicates that the model is able to obtain a good fit to the experimental data when the fluid pressure is taken into account. The approximately linear relationship shows the experimental conditions remain within the low stress linear section of the empirical function.

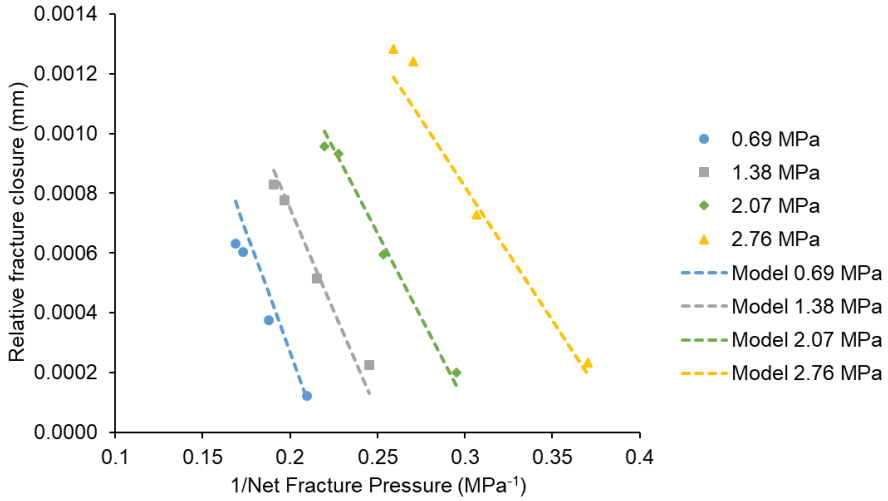

Figure 14: Modelled fits to the experimental data for fracture closure in the heterogeneous resin sample at different downstream pressures (0.69 MPa, 1.38 MPa, 2.07 MPa, 2.76 MPa) using the Goodman model (1976).

In our experiments on the heterogeneous resin the circumferential strain is the same irrespective of the fracture fluid pressure yet the calculated permeability change for a given change in net fracture pressure is different for different fluid pressures. Lamur et al., (2017) tested the impact of effective pressure on fracture permeability by increasing confining stress on fractured samples, a methodology similar to many investigating fracture closure e.g. (Bandis et al., 1983; Barton et al., 1985; Durham, 1997; Gale, 1982; Witherspoon et al., 1980). In these methodologies, the change in fracture aperture with stress is measured directly and records the deformation of the fracture as it is increasingly confined. These experiments record non-linear relationships between permeability and normal stress as a result of increasing contact area and fracture stiffness (e.g. Zimmerman & Main, 2003). In our experiment, the fracture is contained within the specimen so the circumferential strain records any changes in fracture opening/closure with different fluid pressure due to the fractured portion of the sample separating. Figure 13 shows that deformation in response to the changing stress field did occur, but that there is no consistent difference at different fluid pressures.

This suggests that the deformation leading to effective hydraulic aperture change is accommodated within the resin block or on the fracture surface. McCraw et al. (2016) identified a similar behaviour in supercritical CO_2 fracture flow in shales. They interpreted this as high fluid pressures leading to elastic deformation (opening) of the rock matrix between contacting asperities on the fracture surface, which would lead to a change in effective hydraulic aperture in the fracture. A similar process may be in operation here, possibly made more evident due to the low Young's Modulus and absence of permeability for the polyester resin.

It is worth noting that the foregoing discussion is based on an assumption that the stress state locally adjacent to the fracture may be estimated as an average across the width of the fracture, as calculated from a linear elastic finite element model of an intact sample with the experimental loading conditions for boundary conditions. This may not be true, of course, especially as the fracturing process will alter the local stress field in the vicinity of the fracture, and further work is still required to determine the internal stress states in experiments such as ours. A more significant uncertainty in the estimation of internal states of stress is associated with the feedbacks within the system of intact-blocks and fracture(s) that comprise a sample after and during the fracturing process. A full examination of these feedbacks, and thus changes of state, is beyond the scope of this paper. Simulation studies using dis-continuum geo-mechanics methods reveal major changes of local stress states within the intact blocks of rock (Alruwaili et al., 2017), although these concepts are not widely acknowledged in the geoscience literature. Nevertheless, we feel compelled to mention this subject because they indicate there is a convincing need to test such simulation-based ideas about the complexity of stress states within fractured rock masses against experimental data as described in this paper.

6. Conclusions

Our hydraulic fracturing experiments under polyaxial stress conditions show that the fractures induced in these large (193.75 mm diameter) cylindrical samples, composed of homogeneous and heterogeneous, non-porous resin, and a low porosity-permeability greywacke, propagate in both tensile and shear orientations with respect to the polyaxial stress state (caused by differential radial pressures). High resolution circumferential strain data indicate both tensile and shear displacements on the fractures, and show elongation of the sample margin normal to the fracture and contraction on the margin parallel to the propagating fracture. The combination of the fibre optic strain sensors and fluid pressure data reveal that fracture propagation occurs both with fluid pressure drops (unstable) and at constant fluid pressure (stable).

Permeability of the generated fractures is dependent on fracture-normal stress, fracture fluid pressure, and the complete stress state. These novel experiments, based on the ability of the GREAT cell to change both the magnitudes and orientations of the principal stresses while the sample remains *in-situ*, provide the following key findings:

- Average normal stress on the fracture plane (as calculated from a linear elastic finite element model of the applied stress conditions) exerts a primary control on fracture permeability, with higher normal stress reducing fracture permeability as expected.
- Axially aligned hydraulic fractures with a component of shear, oriented at maximum shear stress to the intermediate principal stress, show (elevated) fracture fluid flow characteristics that do not conform to the simple normal stress-permeability relationship.

- The direction of shear displacement is important due to the potential to match or mis-match fracture surface asperities leading to second order control on fracture flow.
- High fracture fluid pressure counteracts fracture closure at low net fracture pressures, characterising a non-linear relationship between net fracture pressure and permeability.

These results demonstrate the unique ability of the GREAT cell to probe the interactions between hydraulic and mechanical processes in fractured samples under polyaxial stress states.

7. Open Research

The data generated from the experiments presented are available from Fraser-Harris et al. (2020).

8. Acknowledgements

The research leading to the development of the GREAT cell and the results presented have been supported by a University of Edinburgh College of Science and Engineering capital equipment grant, internal investment by Heriot Watt University, by the German Science Foundation (Deutsche Forschungsgemeinschaft, DFG, grant: INST 186/1197 - 1 FUGG), and the German Lower Saxony Ministry of Science and Culture (Niedersächsisches Ministerium für Wissenschaft und Kultur, MWK, grant 11 – 76251-10-5/15 (ZN3271)), and by funding from the European Union's Horizon 2020 research and innovation programme under grant agreement No 636811. This project has also received funding from EPSRC Propserity Partnership research and innovation programme under grant No EP/S005560/1.

The authors would also like to extend their thanks and gratitude to George Pratt and Rab Louden at Heriot Watt, as well as Alex Hart and Ivan Febbrari at the University of Edinburgh for their huge contribution to building and commissioning the GREAT cell and general technical advice. The authors would also like to thank Jimmy Smith (University of Edinburgh), Yan Lavallée, Jenny Schauroth, Josh Weaver (all from the University of Liverpool), and Mike Heap and Thierry Reuschlé (Université de Strasbourg) for their help and collaboration in sample preparation and characterisation, especially on such short time-scales and in the midst of a global pandemic.

9. Competing interests statement on behalf of all authors

No competing interests to declare

10. References

Ahmed, S., Müller, T. M., Madadi, M., & Calo, V. (2019). Drained pore modulus and Biot coefficient from pore-scale digital rock simulations. *International Journal of Rock Mechanics and Mining Sciences*, *114*(February 2018), 62–70. https://doi.org/10.1016/j.ijrmms.2018.12.019

Alruwaili, K. M. M. (2016). *Continuum and combined continuum-discontinuum analysis of wellbore mechanics and stimulation response*. Heriot Watt University.

Aly, M. F., Goda, I. G. M., & Hassan, G. a. (2010). Experimental Investigation of the Dynamic Characteristics of Laminated Composite Beams. *International Journal*, *03*, 59–68.

Aybar, U., Eshkalak, M. O., Sepehrnoori, K., & Patzek, T. W. (2014). The effect of natural fracture's closure on long-term gas production from unconventional resources. *Journal of Natural Gas Science and Engineering*, *21*, 1205–1213. https://doi.org/10.1016/j.jngse.2014.09.030

Bahorich, B., Olson, J. E., & Holder, J. (2012). Examining the Effect of Cemented Natural Fractures on Hydraulic Fracture Propagation in Hydrostone Block Experiments. *SPE Annual Technical Conference and Exhibition*. https://doi.org/10.2118/160197-MS

Bai, M., Shen, A., Meng, L., Zhu, J., & Song, K. (2018). Well completion issues for

underground gas storage in oil and gas reservoirs in China. In *Journal of Petroleum Science and Engineering* (Vol. 171, Issue May 2017, pp. 584–591). Elsevier B.V. https://doi.org/10.1016/j.petrol.2018.07.061

Bandis, S. C., Lumsden, A. C., & Barton, N. R. (1983). Fundamentals of rock joint deformation. *International Journal of Rock Mechanics and Mining Sciences And*, *20*(6), 249–268. https://doi.org/10.1016/0148-9062(83)90595-8

Barton, N., Bandis, S., & Bakhtar, K. (1985). Strength, deformation and conductivity coupling of rock joints. *International Journal of Rock Mechanics and Mining Sciences And*, *22*(3), 121–140. https://doi.org/10.1016/0148-9062(85)93227-9

Benson, P. M., Austria, D. C., Gehne, S., Butcher, E., Harnett, C. E., Fazio, M., Rowley, P., & Tomas, R. (2020). Laboratory simulations of fluid-induced seismicity, hydraulic fracture, and fluid flow. *Geomechanics for Energy and the Environment*, *xxxx*, 100169. https://doi.org/10.1016/j.gete.2019.100169

Beugelsdijk, L. J. L., de Pater, C. J., & Sato, K. (2000). Experimental Hydraulic Fracture Propagation in a Multi-Fractured Medium. *SPE Asia Pacific Conference on Integrated Modelling for Asset Management*, 1–8. https://doi.org/10.2523/59419-MS

Birkholzer, J. T., Bond, A. E., Hudson, J. A., Jing, L., Tsang, C.-F., Shao, H., & Kolditz, O. (2018). DECOVALEX-2015: an international collaboration for advancing the understanding and modeling of coupled thermo-hydro-mechanical-chemical (THMC) processes in geological systems. *Environmental Earth Sciences*, *77*(14), 539. https://doi.org/10.1007/s12665-018-7697-7

Blanton, T. L. (1982). An Experimental Study of Interaction Between Hydraulically Induced and Pre-Existing Fractures. *SPE Unconventional Gas Recovery Symposium*. https://doi.org/10.2118/10847-MS

Bossart, P., Meier, P. M., Moeri, A., Trick, T., & Mayor, J. C. (2002). Geological and hydraulic characterisation of the excavation disturbed zone in the Opalinus Clay of the Mont Terri Rock Laboratory. *Engineering Geology*, *66*(1–2), 19–38. https://doi.org/10.1016/S0013-7952(01)00140-5

Chen, Z., Narayan, S. P., Yang, Z., & Rahman, S. S. (2000). An experimental investigation of hydraulic behaviour of fractures and joints in granitic rock. *International Journal of Rock Mechanics and Mining Sciences*, *37*(7), 1061–1071. https://doi.org/10.1016/S1365-1609(00)00039-3

Cheng, L., Rong, G., Yang, J., & Zhou, C. (2017). Fluid Flow Through Single Fractures With Directional Shear Dislocations. *Transport in Porous Media*, *118*(2), 301–326. https://doi.org/10.1007/s11242-017-0861-9

Cheng, Y., & Zhang, Y. (2020). Experimental study of fracture propagation: The application in energy mining. In *Energies* (Vol. 13, Issue 6). https://doi.org/10.3390/en13061411

Chitrala, Y., Moreno, C., Sondergeld, C., & Rai, C. (2013). An experimental investigation into hydraulic fracture propagation under different applied stresses in tight sands using acoustic emissions. *Journal of Petroleum Science and Engineering*, *108*, 151–161. https://doi.org/10.1016/j.petrol.2013.01.002

Chuprakov, D. A., Akulich, A. V, Siebrits, E., Thiercelin, M., & Regional, S. (2010). *Hydraulic Fracture Simulation in Naturally Fractured Reservoirs*. 77042.

de Pater, C. J., & Beugelsdijk, L. J. L. (2005). Experiments and numerical simulation of hydraulic fracturing in naturally fractured rock. *The 40th U.S. Symposium on Rock Mechanics (USRMS): Rock Mechanics for Energy, Mineral and Infrastructure Development in the Northern Regions*.

Diaz, M. B., Kim, K. Y., & Jung, S. G. (2020). Effect of frequency during cyclic hydraulic fracturing and the process of fracture development in laboratory experiments. *International Journal of Rock Mechanics and Mining Sciences*, *134*(July), 104474. https://doi.org/10.1016/j.ijrmms.2020.104474

Durham, W. B. (1997). Laboratory observations of the hydraulic behavior of a permeable fracture from 3800 m depth in the KTB pilot hole. *Journal of Geophysical Research B: Solid Earth*, *102*(B8), 18405–18416. https://doi.org/10.1029/96jb02813

Fan, T. gang, & Zhang, G. qing. (2014). Laboratory investigation of hydraulic fracture networks in formations with continuous orthogonal fractures. *Energy*, *74*(C), 164–173. https://doi.org/10.1016/j.energy.2014.05.037

Fatahi, H., Hossain, M. M., & Sarmadivaleh, M. (2017). Numerical and experimental investigation of the interaction of natural and propagated hydraulic fracture. *Journal of Natural Gas Science and Engineering*, *37*, 409–424. https://doi.org/10.1016/j.jngse.2016.11.054

Fraser-Harris, A., Lightbody, A., Edlmann, K., Elphick, S., Couples, G. D., Sauter, M., & McDermott, C. I. (2020). Sampling and preparation of c.200 mm diameter cylindrical rock samples for geomechanical experiments. *International Journal of Rock Mechanics and Mining Sciences*, *128*(January), 104233. https://doi.org/10.1016/j.ijrmms.2020.104233

Fraser-Harris, A. P., McDermott, C. I., Couples, G. D., Edlmann, K., Lightbody, A., Cartwright-Taylor, A., Kendrick, J. E., Brondolo, F., Fazio, M., & Sauter, M. (2020). *Experimental Invesitgation of Hydraulic Fracturing and Stress Sensitivity of Fracture Permeability under changing Polyaxial Stress Conditions*. 4TU.ResearchData. https://doi.org/10.4121/uuid:ea9282ed-2464-4ec2-82e8-d0d91aa1f770

Fraser Harris, A. P., McDermott, C. I., Kolditz, O., & Haszeldine, R. S. (2015). Modelling groundwater flow changes due to thermal effects of radioactive waste disposal at a hypothetical repository site near Sellafield, UK. *Environmental Earth Sciences*, *74*(2). https://doi.org/10.1007/s12665-015-4156-6

Gale, J. E. (1982). The effects of fracture type (induced versus natural) on the stress-fracture closure-fracture permeability relationships. *American Rock Mechanics Association*, *290*(July), 290–298. https://doi.org/ARMA-82-290

Gaus, I., & Ó Dochartaigh, B. É. (2000). Conceptual modelling of data-scarce aquifers in Scotland: The sandstone aquifers of fife and dumfries. *Geological Society Special Publication*, *182*(1), 157–168. https://doi.org/10.1144/GSL.SP.2000.182.01.15

Gehne, S., Benson, P. M., Koor, N., Dobson, K. J., Enfield, M., & Barber, A. (2019). Seismo-Mechanical Response of Anisotropic Rocks Under Hydraulic Fracture Conditions: New Experimental Insights. *Journal of Geophysical Research: Solid Earth*, *124*(9), 9562–9579. https://doi.org/10.1029/2019JB017342

Gifford, D. K., Kreger, S. T., Sang, A. K., Froggatt, M. E., Duncan, R. G., Wolfe, M. S., & Soller, B. J. (2007). *Swept-wavelength interferometric interrogation of fiber Rayleigh*

scatter for distributed sensing applications. https://doi.org/10.1117/12.734931

Gu, H., Weng, X., Lund, J., MacK, M., Ganguly, U., & Suarez-Rivera, R. (2012). Hydraulic fracture crossing natural fracture at nonorthogonal angles: A criterion and its validation. *SPE Production and Operations*, *27*(1), 20–26. https://doi.org/10.2118/139984-PA

Guo, B., Fu, P., Hao, Y., Peters, C. A., & Carrigan, C. R. (2016). Thermal drawdown-induced flow channeling in a single fracture in EGS. *Geothermics*, *61*, 46–62. https://doi.org/10.1016/j.geothermics.2016.01.004

Guo, F., Morgenstern, N. R., & Scott, J. D. (1993). An experimental investigation into hydraulic fracture propagation-Part 1. Experimental facilities. *International Journal of Rock Mechanics and Mining Sciences And*, *30*(3), 177–188. https://doi.org/10.1016/0148-9062(93)92722-3

Guo, T., Zhang, S., Qu, Z., Zhou, T., Xiao, Y., & Gao, J. (2014). Experimental study of hydraulic fracturing for shale by stimulated reservoir volume. *Fuel*, *128*, 373–380. https://doi.org/10.1016/j.fuel.2014.03.029

Haimson, B. C., & Zhao, Z. (1991). Effect of Borehole Size and Pressurization Rate on Hydraulic Fracturing Breakdown Pressure. *The 32nd U.S. Symposium on Rock Mechanics (USRMS)*.

Heinemann, N., Booth, M. G., Haszeldine, R. S., Wilkinson, M., Scafidi, J., & Edlmann, K. (2018). Hydrogen storage in porous geological formations – onshore play opportunities in the midland valley (Scotland, UK). *International Journal of Hydrogen Energy*, *43*(45), 20861–20874. https://doi.org/10.1016/j.ijhydene.2018.09.149

Hofmann, H., Blöcher, G., Milsch, H., Babadagli, T., & Zimmermann, G. (2016). Transmissivity of aligned and displaced tensile fractures in granitic rocks during cyclic loading. *International Journal of Rock Mechanics and Mining Sciences*, *87*, 69–84. https://doi.org/10.1016/j.ijrmms.2016.05.011

Hofmann, H., Zimmermann, G., Zang, A., & Min, K. B. (2018). Cyclic soft stimulation (CSS): a new fluid injection protocol and traffic light system to mitigate seismic risks of hydraulic stimulation treatments. *Geothermal Energy*, *6*(1). https://doi.org/10.1186/s40517-018-0114-3

Hou, B., Chen, M., Li, Z., Wang, Y., & Diao, C. (2014). Propagation area evaluation of hydraulic fracture networks in shale gas reservoirs. *Petroleum Exploration and Development*, *41*(6), 833–838. https://doi.org/10.1016/S1876-3804(14)60101-4

Hu, L., Ghassemi, A., Pritchett, J., & Garg, S. (2020). Characterization of laboratory-scale hydraulic fracturing for EGS. *Geothermics*, *83*(July 2019), 101706. https://doi.org/10.1016/j.geothermics.2019.07.004

Hubbert, M., & Willis, D. (1957). Mechanics of hydraulic fracturing. *Journal for Petroleum Technology*, *9*(6), 153–166. https://doi.org/10.1016/S0376-7361(07)53011-6

Hudson, J. a., Stephansson, O., & Andersson, J. (2005). Guidance on numerical modelling of thermo-hydro-mechanical coupled processes for performance assessment of radioactive waste repositories. *International Journal of Rock Mechanics and Mining Sciences*, *42*(5–6), 850–870. https://doi.org/10.1016/j.ijrmms.2005.03.018

Iriarte, J., Katsuki, D., Tutuncu, A. N., & Gas, U. N. (2018). Fracture Conductivity, Geochemical, and Geomechanical Monitoring of the Niobrara Formation under Triaxial

Stress State. *Society of Petroleum Engineers Journal*.

Ishida, T., Chen, Q., Mizuta, Y., & Roegiers, J. C. (2004). Influence of fluid viscosity on the hydraulic fracturing mechanism. *Journal of Energy Resources Technology, Transactions of the ASME*, *126*(3), 190–200. https://doi.org/10.1115/1.1791651

Jamison, W., & Azad, A. (2017). The hydraulic fracture – natural fracture network configuration in shale reservoirs: Geological limiting factors. *Journal of Petroleum Science and Engineering*, *159*(September), 205–229. https://doi.org/10.1016/j.petrol.2017.09.017

Kabuth, A., Dahmke, A., Beyer, C., Bilke, L., Dethlefsen, F., Dietrich, P., Duttmann, R., Ebert, M., Feeser, V., Görke, U. J., Köber, R., Rabbel, W., Schanz, T., Schäfer, D., Würdemann, H., & Bauer, S. (2017). Energy storage in the geological subsurface: dimensioning, risk analysis and spatial planning: the ANGUS+ project. *Environmental Earth Sciences*, *76*(1). https://doi.org/10.1007/s12665-016-6319-5

Kamali, A., & Ghassemi, A. (2018). Analysis of injection-induced shear slip and fracture propagation in geothermal reservoir stimulation. *Geothermics*, *76*(October 2017), 93–105. https://doi.org/10.1016/j.geothermics.2018.07.002

Konzuk, J. S., & Kueper, B. H. (2004). Evaluation of cubic law based models describing single-phase flow through a rough-walled fracture. *Water Resources Research*, *40*(2), 1–17. https://doi.org/10.1029/2003WR002356

Kulatilake, P. H. S. W., Park, J., Balasingam, P., & Morgan, R. (2008). Quantification of aperture and relations between aperture, normal stress and fluid flow for natural single rock fractures. *Geotechnical and Geological Engineering*, *26*(3), 269–281. https://doi.org/10.1007/s10706-007-9163-2

Lamur, A., Kendrick, J. E., Eggertsson, G. H., Wall, R. J., Ashworth, J. D., & Lavallée, Y. (2017). The permeability of fractured rocks in pressurised volcanic and geothermal systems. *Scientific Reports*, *7*(1), 1–9. https://doi.org/10.1038/s41598-017-05460-4

Lee, H. P., Olson, J. E., Holder, J., Gale, J. F. W., & Myers, R. D. (2014). *Journal of Geophysical Research : Solid Earth fractures with preexisting discontinuities in shale*. 169–181. https://doi.org/10.1002/2014JB011358.Received

Lee, H. S., & Cho, T. F. (2002). Hydraulic characteristics of rough fractures in linear flow under normal and shear load. *Rock Mechanics and Rock Engineering*, *35*(4), 299–318. https://doi.org/10.1007/s00603-002-0028-y

Lee, S. F. (2002). *Viscoelastic behaviour of Poly(methyl methacrylate) and Polystyrene*. Loughborough University.

Lei, Q., Wang, X., Xiang, J., & Latham, J. (2017). *Polyaxial stress-dependent permeability of a three-dimensional fractured rock layer*. 2251–2262. https://doi.org/10.1007/s10040-017-1624-y

Lockner, D. A., & Byerlee, J. D. (1977). Hydrofracture in Weber Sandstone at high confining pressure and differential stress. *Journal of Geophysical Research*, *82*(14), 2018–2026. https://doi.org/10.1029/JB082i014p02018

Mack, M. G. (2016). The Effects of Stress Changes and Natural Fractures on Hydraulic Fracture Interactions. *American Rock Mechanics Association*.

1425 Mattila, J., & Follin, S. (2019). Does In Situ State of Stress Affect Fracture Flow in
1426 Crystalline Settings? *Journal of Geophysical Research: Solid Earth*, *124*(5), 5241–5253.
1427 https://doi.org/10.1029/2018JB016791

1428 McClure, M. W., & Horne, R. N. (2014). An investigation of stimulation mechanisms in
1429 Enhanced Geothermal Systems. *International Journal of Rock Mechanics and Mining*
1430 *Sciences*, *72*, 242–260. https://doi.org/10.1016/j.ijrmms.2014.07.011

1431 McCraw, C., Edlmann, K., Miocic, J., Gilfillan, S., Haszeldine, R. S., & McDermott, C. I.
1432 (2016). Experimental investigation and hybrid numerical analytical hydraulic
1433 mechanical simulation of supercritical CO2 flowing through a natural fracture in
1434 caprock. *International Journal of Greenhouse Gas Control*, *48*, 120–133.
1435 https://doi.org/10.1016/j.ijggc.2016.01.002

1436 McDermott, C., Bond, A., Fraser Harris, A., Chittenden, N., & Thatcher, K. (2015).
1437 Application of hybrid numerical and analytical solutions for the simulation of coupled
1438 thermal, hydraulic, mechanical and chemical processes during fluid flow through a
1439 fractured rock. *Environmental Earth Sciences*, *74*(12), 7837–7854.
1440 https://doi.org/10.1007/s12665-015-4769-9

1441 McDermott, C. I., Fraser-Harris, A. P., Sauter, M., Couples, G. D., Edlmann, K. P., Kolditz,
1442 O., Lightbody, A., Somerville, J., & Wang, W. (2018). New Experimental Equipment
1443 Recreating Geo-Reservoir Conditions in Large, Fractured, Porous Samples to
1444 Investigate Coupled Thermal, Hydraulic and Polyaxial Stress Processes. *Scientific*
1445 *Reports*, *8*(1), 14549. https://doi.org/10.1038/s41598-018-32753-z

1446 McDermott, C. I., Randriamanjatosoa, A. R. L., Tenzer, H., & Kolditz, O. (2006). Simulation
1447 of heat extraction from crystalline rocks: The influence of coupled processes on
1448 differential reservoir cooling. *Geothermics*, *35*(3), 321–344.
1449 https://doi.org/10.1016/j.geothermics.2006.05.002

1450 McDermott, C., Williams, J., Tucker, O., Jin, M., Mackay, E., Edlmann, K., Haszeldine, R.
1451 S., Wang, W., Kolditz, O., & Akhurst, M. (2016). Screening the geomechanical stability
1452 (thermal and mechanical) of shared multi-user CO2storage assets: A simple effective
1453 tool applied to the Captain Sandstone Aquifer. *International Journal of Greenhouse Gas*
1454 *Control*, *45*, 43–61. https://doi.org/10.1016/j.ijggc.2015.11.025

1455 Meng, C., & De Pater, C. J. (2011). Acoustic monitoring of hydraulic fracture propagation in
1456 pre-fractured natural rocks. *Key Engineering Materials*, *452–453*(January 2010), 833–
1457 836. https://doi.org/10.4028/www.scientific.net/KEM.452-453.833

1458 Pape, H., Clauser, C., & Iffland, J. (2000). Variation of permeability with porosity in
1459 sandstone diagenesis interpreted with a fractal pore space model. *Pure and Applied*
1460 *Geophysics*, *157*(4), 603–619. https://doi.org/10.1007/pl00001110

1461 Patel, S. M., Sondergeld, C. H., & Rai, C. S. (2017). Laboratory studies of hydraulic
1462 fracturing by cyclic injection. *International Journal of Rock Mechanics and Mining*
1463 *Sciences*, *95*(August 2016), 8–15. https://doi.org/10.1016/j.ijrmms.2017.03.008

1464 Pyrak-Nolte, L., Myer, L., Cook, N. G. W., & Witherspoon, P. (1987). Hydraulic And
1465 Mechanical Properties of Natural Fractures In Low Permeability Rock. *6th ISRM*
1466 *Congress, Montreal, Canada*. https://doi.org/6CONGRESS-1987-042

1467 Renshaw, C.E., & Pollard, D. D. (1995). An experimentally verified criterion for propagation
1468 across unbounded frictional interfaces in brittle, linear elastic materials. *International*

Journal of Rock Mechanics and Mining Sciences & Geomechanics Abstracts, *32*(3), 237–249. https://doi.org/10.1016/0148-9062(94)00037-4

Renshaw, Carl E. (1995). On the relationship between mechanical and hydraulic apertures in rough-walled fractures. *Journal of Geophysical Research*, *100*, 629–636.

Rinaldi, A. P., & Rutqvist, J. (2019). Joint opening or hydroshearing? Analyzing a fracture zone stimulation at Fenton Hill. *Geothermics*, *77*(December 2017), 83–98. https://doi.org/10.1016/j.geothermics.2018.08.006

Rutter, E. H., & Mecklenburgh, J. (2018). Influence of Normal and Shear Stress on the Hydraulic Transmissivity of Thin Cracks in a Tight Quartz Sandstone, a Granite, and a Shale. *Journal of Geophysical Research: Solid Earth*, *123*(2), 1262–1285. https://doi.org/10.1002/2017JB014858

Sarmadivaleh, M., & Rasouli, V. (2014). Test Design and Sample Preparation Procedure for Experimental Investigation of Hydraulic Fracturing Interaction Modes. *Rock Mechanics and Rock Engineering*, *48*(1), 93–105. https://doi.org/10.1007/s00603-013-0543-z

Sarmadivaleh, Mohammad. (2012). Experimental and Numerical Study of Interaction of a Pre-Existing Natural Interface and an Induced Hydraulic Fracture. *PhD Thesis*, *C*(January 2012), 157. https://doi.org/10.13140/RG.2.1.1286.2882

Shen, H., Zhang, Q., Li, Q., Li, X., Shi, L., & Shen, N. (2020). Experimental and Numerical Investigations of the Dynamic Permeability Evolution of a Fracture in Granite During Shearing Under Different Normal Stress Conditions. *Rock Mechanics and Rock Engineering*, *0123456789*. https://doi.org/10.1007/s00603-020-02074-7

Solberg, P., Lockner, D., & Byerlee, J. (1977). Shear and tension hydraulic fractures in low permeability rocks. *Pure and Applied Geophysics PAGEOPH*, *115*(1–2), 191–198. https://doi.org/10.1007/BF01637103

Stanchits, S., Burghardt, J., & Surdi, A. (2015). Hydraulic Fracturing of Heterogeneous Rock Monitored by Acoustic Emission. *Rock Mechanics and Rock Engineering*, *48*(6), 2513–2527. https://doi.org/10.1007/s00603-015-0848-1

Tan, P., Jin, Y., Han, K., Hou, B., Guo, X., Gao, J., & Wang, T. (2017). Analysis of hydraulic fracture initiation and vertical propagation behavior in laminated shale formation. *Fuel*, *206*, 482–493. https://doi.org/10.1016/j.fuel.2017.05.033

Tomac, I., & Sauter, M. (2018). A review on challenges in the assessment of geomechanical rock performance for deep geothermal reservoir development. *Renewable and Sustainable Energy Reviews*, *82*(October 2017), 3972–3980. https://doi.org/10.1016/j.rser.2017.10.076

Vogler, D., Amann, F., Bayer, P., & Elsworth, D. (2016). Permeability Evolution in Natural Fractures Subject to Cyclic Loading and Gouge Formation. *Rock Mechanics and Rock Engineering*, *49*(9), 3463–3479. https://doi.org/10.1007/s00603-016-1022-0

Warpinski, N. R., Clark, J. A., Schmidt, R. A., & Huddle, C. W. (1982). Laboratory Investigation on the -Effect of In-Situ Stresses on Hydraulic Fracture Containment. *Society of Petroleum Engineers Journal*, *22*(03), 333–340. https://doi.org/10.2118/9834-PA

Witherspoon, P. A., Wang, J. S. Y., Iwai, K., & Gale, J. E. (1980). Validity of Cubic Law for fluid flow in a deformable rock fracture. *Water Resources Research*, *16*(6), 1016–1024.

https://doi.org/10.1029/WR016i006p01016

Xu, D., Hu, R., Gao, W., & Xia, J. (2015). Effects of laminated structure on hydraulic fracture propagation in shale. *Petroleum Exploration and Development*, *42*(4), 573–579. https://doi.org/10.1016/S1876-3804(15)30052-5

Ye, Z., & Ghassemi, A. (2018). Injection-Induced Shear Slip and Permeability Enhancement in Granite Fractures. *Journal of Geophysical Research: Solid Earth*, *123*(10), 9009–9032. https://doi.org/10.1029/2018JB016045

Ye, Z., & Ghassemi, A. (2019). Injection-Induced Propagation and Coalescence of Preexisting Fractures in Granite Under Triaxial Stress. *Journal of Geophysical Research: Solid Earth*, *124*(8), 7806–7821. https://doi.org/10.1029/2019JB017400

Zhang, Z., & Nemcik, J. (2013). Fluid flow regimes and nonlinear flow characteristics in deformable rock fractures. *Journal of Hydrology*, *477*, 139–151. https://doi.org/10.1016/j.jhydrol.2012.11.024

Zhou, J., Chen, M., Jin, Y., & Zhang, G. (2008). Analysis of fracture propagation behavior and fracture geometry using a tri-axial fracturing system in naturally fractured reservoirs. *International Journal of Rock Mechanics and Mining Sciences*, *45*(7), 1143–1152. https://doi.org/10.1016/j.ijrmms.2008.01.001

Zhou, J. Q., Hu, S. H., Fang, S., Chen, Y. F., & Zhou, C. B. (2015). Nonlinear flow behavior at low Reynolds numbers through rough-walled fractures subjected to normal compressive loading. *International Journal of Rock Mechanics and Mining Sciences*, *80*, 202–218. https://doi.org/10.1016/j.ijrmms.2015.09.027

Zhuang, L, Kim, K. ., Shin, H. ., Jung, S. ., & Diaz, M. (2018). Experimental Investigation of Effects of Borehole Size and Pressurization Rate on Hydraulic Fracturing Breakdown Pressure of Granite. *ISRM International Symposium -10th Asian Rock Mechanics Symposium*.

Zhuang, Li, Jung, S. G., Diaz, M., Kim, K. Y., Hofmann, H., Min, K. B., Zang, A., Stephansson, O., Zimmermann, G., & Yoon, J. S. (2020). Laboratory True Triaxial Hydraulic Fracturing of Granite Under Six Fluid Injection Schemes and Grain-Scale Fracture Observations. *Rock Mechanics and Rock Engineering*. https://doi.org/10.1007/s00603-020-02170-8

Zhuang, Li, Kim, K. Y., Jung, S. G., Diaz, M., Min, K. B., Zang, A., Stephansson, O., Zimmermann, G., Yoon, J. S., & Hofmann, H. (2019). Cyclic hydraulic fracturing of pocheon granite cores and its impact on breakdown pressure, acoustic emission amplitudes and injectivity. *International Journal of Rock Mechanics and Mining Sciences*, *122*(August). https://doi.org/10.1016/j.ijrmms.2019.104065

Zimmerman, R., & Main, I. (2003). Chapter 7 Hydromechanical Behavior of Fractured Rocks. *International Geophysics*, *89*(C), 363–421. https://doi.org/10.1016/S0074-6142(03)80023-2

Zimmerman, R. W., & Bodvarsson, G. S. (1996). Hydraulic conductivity of rock fractures. *Transport in Porous Media*, *23*(1), 1–30. https://doi.org/10.1007/BF00145263

Zoback, M. D., Rummel, F., Jung, R., & Raleigh, C. B. (1977). Laboratory hydraulic fracturing experiments in intact and pre-fractured rock. *International Journal of Rock Mechanics and Mining Sciences And*, *14*(2), 49–58. https://doi.org/10.1016/0148-

9062(77)90196-6